The Astrophysical Journal, 751:74 (26pp), 2012 May 20 doi:10.1088/0004-637X/751/1/74

THE RECENT STELLAR ARCHEOLOGY OF M31—THE NEAREST RED DISK GALAXY*

T. J. Davidge[1], A. W. McConnachie[1], M. A. Fardal[2], J. Fliri[3], D. Valls-Gabaud[3], S. C. Chapman[4], G. F. Lewis[5], and R. M. Rich[6]

[1] Herzberg Institute of Astrophysics, National Research Council of Canada, 5071 West Saanich Road, Victoria, BC V9E 2E7, Canada
[2] Department of Astronomy, University of Massachusetts, LGRT 619-E, Amherst, MA 01003-9305, USA
[3] LERMA, UMR CNRS 8112, Observatoire de Paris, 61 Avenue de l'Observatoire, 75014 Paris, France
[4] Institute of Astronomy, University of Cambridge, Madingley Road, Cambridge CB3 0HA, UK
[5] Sydney Institute for Astronomy, School of Physics, A28, The University of Sydney, NSW 2006, Australia
[6] Division of Astronomy and Astrophysics, University of California, Los Angeles, 430 Portola Plaza, Box 951547, Los Angeles, CA 90095-1547, USA
Received 2012 January 21; accepted 2012 March 26; published 2012 May 7

ABSTRACT

We examine the star-forming history of the M31 disk during the past few hundred Myr. The luminosity functions (LFs) of main-sequence stars at distances $R_{GC} > 21$ kpc (i.e., >4 disk scale lengths) are matched by models that assume a constant star formation rate (SFR). However, at smaller R_{GC} the LFs suggest that during the past ∼10 Myr the SFR was 2–3 times higher than during the preceding ∼100 Myr. The rings of cool gas that harbor a significant fraction of the current star-forming activity are traced by stars with ages ∼100 Myr, indicating that (1) these structures have ages of at least 100 Myr and (2) stars in these structures do not follow the same relation between age and random velocity as their counterparts throughout the disks of other spiral galaxies, probably due to the inherently narrow orbital angular momentum distribution of the giant molecular clouds in these structures. The distribution of evolved red stars is not azimuthally symmetric, in the sense that the projected density along the northeast segment of the major axis is roughly twice that on the opposite side of the galaxy. The northeast arm of the major axis thus appears to be a fossil star-forming area that dates to intermediate epochs. Such a structure may be the consequence of interactions with a companion galaxy.

Key words: galaxies: evolution – galaxies: individual (M31) – galaxies: spiral

Online-only material: color figures

1. INTRODUCTION

As the nearest large spiral galaxy, M31 is a fundamental benchmark for studies of disk evolution, and our understanding of the evolution of M31 has changed profoundly during the past decade. There is a large body of evidence (e.g., Ibata et al. 2001, 2007; Hammer et al. 2007; Tanaka et al. 2010) that interactions with companion galaxies, some of which may not have survived intact to the present day and remain only as debris trails, have occurred throughout the history of M31. The detection of similar tidal features close to other nearby galaxies (e.g., Martinez-Delgado et al. 2010) indicates that galaxy–galaxy encounters in the local universe have not been rare and have played a key role in sculpting the current appearance of many nearby galaxies.

The current study focuses on investigating the star-forming history (SFH) of M31 during the past few hundred Myr, using the brightest resolved stars as tracers. It has been suggested that M31 has interacted with some of its companions during this time, and a key element of our work is to search for observational signatures of this activity. A review that considers the entire history of M31 will guide our understanding of its present-day appearance and allow a conceptual picture of the key events that shaped its evolution to be developed. To this end, in the remainder of this section we review previous work on the evolution of M31. While current theories for the buildup of disk galaxies give primacy to the smooth accretion of hot and cold gas, the following focuses on the influence of major and minor mergers, as these imprint observable signatures on the kinematics, spatial distribution, and age distribution of stars. Not every interaction can be traced in detail, especially those that happened more than a few dynamical times in the past, and the discussion of the earliest phases of the evolution of M31 are—by necessity—more speculative than the discussion of the most recent events. The ages listed in what follows should also be viewed as approximations.

1.1. Initial Assembly ($t = 10$ Gyr Ago)

The initial assembly of M31 likely involved the merger of proto-galactic structures, which contained a mix of gas and stars that had formed in situ (e.g., Oser et al. 2010). The gas in these structures probably contributed to the assembly of an M31 proto-disk, supplementing material accreted through the large-scale inflow of hot and cold gas. Any early disk was likely short-lived due to the high frequency of major mergers. In addition to disrupting the early disk, mergers may also have spurred the formation of a classical metal-poor halo, through the displacement of stars out of the disk plane. Stars ejected in such events are expected to dominate the central 20 kpc of halos (Zolotov et al. 2009). At larger radii the majority of halo stars may not have had such a violent origin and may instead have been accreted from companion galaxies during the first few Gyr of galaxy assembly (Font et al. 2008; Zolotov et al. 2009; Cooper et al. 2010). A classical metal-poor halo has been detected around M31 (e.g., Kalirai et al. 2006; Chapman et al. 2006; Ibata et al. 2007; Koch et al. 2008).

There is evidence that M31 accreted a number of satellites early on. The integrated luminosities, masses ($\sim 10^9\ M_\odot$), and dynamical properties of the M31 and the Galactic halos are

* Based on observations obtained with MegaPrime/MegaCam, a joint project of CFHT and CEA/DAPNIA, at the Canada–France–Hawaii Telescope (CFHT), which is operated by the National Research Council (NRC) of Canada, the Institut National des Sciences de l'Univers of the Centre National de la Recherche Scientifique (CNRS) of France, and the University of Hawaii.

similar (Chapman et al. 2006; Ibata et al. 2007), and the properties of Galactic globular clusters suggest that six to eight satellites large enough to form large star clusters may have been accreted (e.g., MacKey & Gilmore 2004; Forbes & Bridges 2010). Globular clusters in the M31 halo tend to be associated with tidal debris (Mackey et al. 2010), and the range of ages, chemical mixtures, and overall metallicities among M31 clusters (e.g., Beasley et al. 2005) hints at diverse progenitors. Some objects that were originally identified as globular clusters may not be simple stellar populations (SSPs) (e.g., Davidge et al. 1991; Meylan et al. 2001; Fuentes-Carrera et al. 2008), but instead may be the remnants of dwarf galaxies that were shredded early in the evolution of M31 (Fuentes-Carrera et al. 2008). The properties of classical globular clusters suggest that M31 and the Galaxy may have experienced different chemical enrichment histories early on. When compared with Galactic globular clusters, the spectra of many M31 globular clusters have relatively strong CN absorption bands (e.g., Burstein et al. 1984; Davidge 1990a), and this has been attributed to a comparatively large nitrogen abundance in M31 clusters (Burstein et al. 2004). Such an abundance difference may have its origins in the numbers of present-day stars in globular clusters that formed in the diffuse proto-cluster environments, as opposed to those that formed in the more compact potential wells that existed after cluster formation (Carretta et al. 2010), in the sense that M31 clusters are made up of a smaller fraction of progenitor stars. If correct, then the location of stars in M31 globular clusters on the [Na/Fe] versus [O/Fe] diagram, which is a diagnostic of the rate of chemical enrichment, should differ from that defined by Galactic objects.

Early merger activity likely also produced a pressure-supported bulge (e.g., Bekki & Chiba 2001). Aside from the central few arcseconds, the integrated spectrum of the M31 bulge at visible wavelengths originates predominantly from old stars (e.g., Davidge 1997; Puzia et al. 2005; Saglia et al. 2010). The brightest asymptotic giant branch (AGB) stars are well mixed throughout the central ∼1 kpc of the M31 bulge, as expected if they formed during a rapid, uniform star-forming episode (Davidge 2001b), such as would result from the violent merging of satellites. Still, the structural (e.g., Beaton et al. 2007) and kinematic (e.g., Morrison et al. 2011) properties of the M31 bulge suggest that secular processes may have also contributed to its growth.

The material from which stars in the Galactic bulge formed may have been chemically enriched by the earliest generation of globular clusters (Davidge 2001a). If globular clusters did play a significant role in enriching the early interstellar medium (ISM) of M31, then the chemical properties of stars in the bulge and globular clusters may show similarities. In fact, the strengths of CN absorption bands at visible wavelengths in the integrated spectrum of the inner bulge of M31 are reminiscent of those in M31 globular clusters (Davidge 1997), suggesting a chemical kinship.

A thick disk may also have been formed during the early assembly of M31. Using kinematic selection criteria, Collins et al. (2011) detect a thick disk in M31 and find that the component stars are 0.2–0.3 dex more metal-poor than thin-disk stars at the same galactic radius. The estimated total mass of the thick disk suggests that it did not form from the destruction of a satellite that follows the trend between [M/H] and total mass defined by present-day systems. If the M31 thick disk formed from thin-disk stars that were kinematically heated, then its (comparatively) low metallicity suggests that this happened during early epochs, before the major merger that produced the extended extraplanar component discussed in the next section.

The spatial extent of M31 at the end of its initial assembly was significantly smaller than the present-day galaxy. Simulations suggest that a galaxy with a present-day mass like that of M31 probably accreted no more than one-half of this mass by moderate redshifts (Stewart et al. 2008), while at $z \sim 2$ the spatial extent of its disk may have been substantially (by a factor of roughly two-thirds) smaller than its present-day value (Firmani & Avila-Reese 2009). The modest size of the M31 progenitor aside, it was this system that served as the seed for the subsequent evolution that led to the present-day galaxy.

1.2. The Formation of the Present-day Disk ($t = 8$ Gyr Ago)

Mergers were common events during intermediate epochs and played a key role in sculpting the morphological properties of nearby disk galaxies (Hammer et al. 2007, 2009; van der Kruit & Freeman 2011). Simulations of a merger between a disk galaxy and a large companion find that the existing disk can be obliterated, with the orbits of disk stars thermalizing to form a pressure-supported extraplanar population (e.g., Hopkins et al. 2009). A gas disk will re-form if the progenitors have sufficient quantities of gas (Robertson et al. 2006; Governato et al. 2007).

There is evidence that a violent merger occurred only a few Gyr following the initial assembly of M31. Such an event would have profoundly affected the morphology of M31, and may even have produced features that are usually attributed to more recent interactions (Hammer et al. 2010). The proposed merger heated the disk of M31 and produced a diffuse extraplanar component that is distinct from the classical metal-poor halo. It has long been known that the extraplanar regions of M31 are dominated by stars with metallicities that (1) are much higher than those in the Galactic halo (e.g., Mould & Kristian 1986; Pritchet & van den Bergh 1988; Durrell et al. 2001) and (2) are consistent with an origin in either a large disk or a Small Magellanic Cloud/Large Magellanic Cloud (SMC/LMC) like companion. More recently, a kinematically hot component (e.g., Chapman et al. 2006; Gilbert et al. 2007) has been detected, which has been traced out to extraplanar distances of 60 kpc. This component is distinct from the thick disk, which has a vertical scale height of 3 kpc (Collins et al. 2011). The metallicities of stars in this component show little or no trend with distance from the galaxy (Chapman et al. 2006; Koch et al. 2008; Richardson et al. 2009). A break in the surface brightness profile occurs near 30 kpc (Ibata et al. 2007), possibly indicating the transition between a violently disturbed inner halo and a more metal-poor classical halo. The lack of sub-structure in the distribution of the moderately metal-rich extraplanar stars suggests that they are not the remnants of a galaxy that was slowly accreted by M31, but instead are the result of a kinematically violent event.

The extraplanar component must have an age of at least a few Gyr, as the C/M5+ ratio is 0.10 ± 0.05 throughout the outer regions of M31 (Koch & Rich 2010). Such a C star frequency among stars with a moderately sub-solar metallicity is suggestive of an age in excess of ∼3–6 Gyr (e.g., Cole & Weinberg 2002). Brown et al. (2008) discuss observations of extraplanar fields with minor-axis distances of 21 and 35 kpc, which are populated by stars with main-sequence turnoff

(MSTO) ages $\geqslant$8 Gyr.[7] The age distribution is such that the majority of stars in the 35 kpc field are not associated with the early assembly of M31, as only 10% are extremely old and metal-poor and so likely belong to the classical halo. That the bulk of the stars in the two Brown et al. (2008) fields have ages >8 Gyr argues that (1) the merger occurred a few Gyr after the initial assembly of M31 and (2) there has not been a subsequent merger of comparable magnitude—while M31 has likely been subject to encounters with other galaxies in the more recent past (see below), none of these have been as disruptive as the event described here.

A star formation rate (SFR) for M31 during this epoch can be estimated from the relation between the brightness of the brightest globular cluster, normalized to an age of 10 Myr, and SFR. The most luminous globular cluster that is known to have formed during intermediate epochs is 292-010, for which Beasley et al. (2004) find a mass of $1.7 \times 10^5\ M_\odot$. The models of Bruzual & Charlot (2003) indicate that $\log(M/L)_V \sim -1.5$ for a population with an age 10 Myr, and so 292-010 would have had $M_V = -16.8$ when it was 10 Myr old. Applying relation (1) from Bastian (2008) yields an SFR of $\sim$320 $M_\odot$ yr^{-1}.

Major mergers trigger large-scale star-forming activity that is not restricted to the central regions of the galaxy (e.g., Teyssier et al. 2010), and M31 may have appeared as an ultraluminous infrared galaxy (ULIRG) for a period of time during intermediate epochs. Star formation is seen throughout the disks of ULIRGs and is curtailed at progressively smaller radii as torques cause gas to move inward (e.g., Soto & Martin 2010). If M31 was a typical ULIRG, then 5%–10% of its current stellar mass may have been produced over a $\sim$0.1 Gyr (Marcillac et al. 2006) time span, and this is roughly consistent with the SFR estimated above from the brightest intermediate-age globular cluster.

The formation of globular clusters in the local universe is associated with the large-scale re-distribution of gas that occurs during major mergers (e.g., Whitmore et al. 1993) and the concomitant violent turbulent stirring of the ISM that produces dense star-forming clumps (Teyssier et al. 2010). Globular clusters in M31 span a wide range of ages (e.g., Beasley et al. 2004; Burstein et al. 2004; Fusi Pecci et al. 2005; Caldwell et al. 2009), and Puzia et al. (2005) find peaks in the cluster age distribution at $t \sim 12$ Gyr, 8 Gyr, and 1 Gyr. The majority of globular clusters in M31 belong to the oldest age group, which is associated with the initial assembly of the galaxy. However, the number of clusters that belong to the 8 Gyr peak—and which likely formed during the major merger that produced the extraplanar component—is a significant fraction of the older cluster system. These intermediate-age clusters tend to be seen against the disk of the galaxy and are not at large radii. To the extent that globular clusters are probes of a disturbed and turbulent ISM, the 8 Gyr cluster population is the remnant of an event that was almost as violent as the mergers associated with the initial assembly of M31.

A major merger would have imprinted signatures on the age distribution of stars throughout much of the disk. If the present-day disk of M31 formed during intermediate epochs following the obliteration of an earlier disk, then there should be (1) an absence of disk stars with ages >8 Gyr and (2) a large population of disk stars that formed $\sim$8 Gyr in the past—these are the field counterpart of the globular cluster population that formed at that time. In addition, starbursts deplete the gas supply at a rate that is an order of magnitude shorter than in a normal disk (Daddi et al. 2010). Therefore, the SFR would have plunged within a few disk rotation times of the merger.

Observations that fully test these predictions require photometric depths and angular resolutions that tax the capabilities of existing telescopes. Still, Olsen et al. (2006) investigate the SFH of bulge and disk fields in M31 and find a preponderance of stars with ages $\geqslant$8 Gyr. This is consistent with the disk of M31 experiencing a large burst of star formation in the past that may not have been associated with the epoch of earliest disk assembly.

1.3. A Close Encounter with M33 (t = 2–4 Gyr Ago)

M31 has not evolved in isolation since the major merger that spurred the formation of the present-day thin disk, and there is a high probability that there was a close encounter between M31 and M33 during intermediate epochs. Various studies have estimated when such an interaction may have occurred. The SFH of M33 suggests that the encounter must have happened at least 0.5 Gyr in the past (Davidge & Puzia 2011). Using the locations and velocities of M31 and M33, Putman et al. (2009) argue that an encounter occurred 1–3 Gyr in the past, while Bekki (2008) assigns an age of 4–8 Gyr based on the properties of the H I bridge that may link the galaxies (Braun & Thilker 2004). Simulations discussed by McConnachie et al. (2009) that use currently available orbital constraints and the assumption that M33 was significantly perturbed by the encounter place this interaction a few billion years in the past.

There is a high probability that the tidal radius of M33 was $\leqslant$15 kpc during this encounter, and this would have disturbed the disk of M33. The S-shaped H I distribution in the outer regions of M33 is testament of such a disturbance, and this structure likely contains gas that was stripped from the M33 disk (Putman et al. 2009). The detection of extended stellar structures in the outer regions of the M33 disk, coupled with isophotal distortions at smaller radii, provides further evidence that the disk of M33 was disturbed (McConnachie et al. 2010; Davidge & Puzia 2011).

The disk of M31 would also have been affected by this event (McConnachie et al. 2009; Davidge & Puzia 2011), with elevated levels of star-forming activity being sparked as tidal forces re-distributed gas. Intermediate-age globular clusters in M31 with ages $\sim$2 Gyr (Puzia et al. 2005) may have formed during this event. While the SFR of the M31 disk would have been greatly elevated immediately after the encounter, it would eventually drop as the ISM is depleted and disrupted. There is evidence of a decrease in M31 star-forming activity $\sim$1 Gyr ago (Williams 2002). Given that the damping timescale for elevated SFRs is on the order of a few disk crossing times, the drop in the SFR found by Williams (2002) is consistent with an interaction that had peak star-forming activity $\sim$2 Gyr ago.

If gas was re-distributed throughout M31, then intense star-forming activity would likely have been triggered in the galaxy center, and this part of M31 *does* contain stars that formed at a time that coincides with the proposed interaction with M33. The integrated spectrum of the central few arcseconds of M31 at visible wavelengths reveals a large population of objects with an age of a few Gyr (Davidge 1997; Sil'chenko et al. 1998). Saglia et al. (2010) conclude from integrated spectra that the luminosity-weighted age of stars near the center of M31 is 4–8 Gyr.

[7] A field that is 11 kpc above the disk was also observed by Brown et al. (2008). The stars in that field tend to have ages $\geqslant$4 Gyr, with a modest number of younger objects. The majority of stars in the 11 kpc field are probably not part of a pressure-supported system but are likely associated with the disk (e.g., Ibata et al. 2007).

1.4. The Recent Past ($t < 2$ Gyr Ago)

Mergers and interactions with companions that have $\leqslant 10\%$ the mass of the primary galaxy are not expected to permanently disrupt disks (e.g., Stewart et al. 2008), and there is evidence that M31 has interacted with companions in this mass range during recent epochs. The most overt signature of such an encounter may be the giant stellar stream (GSS; Ibata et al. 2001). The GSS is a substantial structure with the northern and southern ends separated by at least 130 kpc along the line of sight (McConnachie et al. 2003).

The stellar content of the GSS suggests that the progenitor was a massive dwarf galaxy, and Ibata et al. (2001) discuss NGC 205 and M32 as possible sources. The photometric properties of red giant branch (RGB) stars in the GSS are indicative of a moderately metal-rich system, with a 0.5 dex dispersion in [M/H] (McConnachie et al. 2003). Using the red clump of core helium-burning stars as an age indicator, Tanaka et al. (2010) conclude that stars in the GSS have an age near 7 Gyr and a peak [M/H] near −0.3. This metallicity is comparable to that of stars in the LMC and suggests a progenitor mass $\sim 10^9$–$10^{10}\ M_\odot$. Fardal et al. (2007) and Ibata et al. (2007) arrive at similar progenitor mass estimates. Upper limits to the mass of the progenitor can also be placed. Assuming that the GSS progenitor passed through the disk of M31, Mori & Rich (2008) conclude that it must have had a mass $< 10^{10}\ M_\odot$ so as not to widen the disk of M31 more than is observed.

Font et al. (2006) conclude that the encounter that formed the GSS occurred only a few hundred Myr in the past, while Mori & Rich (2008) assign an age ∼1 Gyr. The age predicted for the GSS by Font et al. (2006) is similar to that modeled by Block et al. (2006) for the supposed passage of a satellite (presumably M32) through the M31 disk. The mean metallicity of stars in the outer regions of M32 is roughly −0.25 (Rose et al. 2005), which is consistent with the metallicity of stars in the GSS.

Models that attempt to reproduce the orbital properties of the GSS predict that the encounter occurred much more recently than might be inferred from its stellar content. The timings predicted by kinematic studies and the ages of stars in the GSS are only in conflict if the progenitor contained a reservoir of cool gas that could have fueled star formation up to the time of its disruption. If the progenitor was depleted of gas a few Gyr in the past–and most present-day companions of M31, such as M32, are gas-depleted (e.g., Welch et al. 1998; Sage et al. 1998; Grcevich & Putman 2009)—then there is a clear physical explanation for the apparent conflict between the kinematic and stellar content age estimates.

The extraplanar regions of M31 are laced with stellar streams and tidal structures, some of which may or may not be related to the GSS. The completeness of the catalog of these structures is uncertain, as there is a bias against the detection of metal-poor and/or old features. This bias occurs because higher surface brightness structures tend to have higher metallicities and/or formed more recently (e.g., Gilbert et al. 2009).

The diverse stellar contents of streamlets along the minor axis of M31 led Ibata et al. (2007) to suggest that these structures have multiple progenitors, all of which—based on metal content—would have initially been larger than the Fornax dwarf spheroidal. Mori & Rich (2008) find that a single minor merger can pollute a large fraction of the extraplanar regions of M31 within ∼2 Gyr of an encounter. Still, they also find that some structures in the outer regions of M31 likely formed more than 3–4 Gyr in the past and so are not related in a direct way to the GSS, to which they assign an age of 1 Gyr. Fardal et al. (2008), Tanaka et al. (2010), and Hammer et al. (2010) argue that many features in the outer regions of M31 could result from an interaction between M31 and a single galaxy. The stream-to-stream diversity in stellar contents indicates that a progenitor that produces multiple observed streams would likely have had a metallicity gradient, and such gradients are seen in nearby Local Group dwarf galaxies (e.g., Harbeck et al. 2001).

Clues of a significant accretion event within the past few hundred Myr also lurk in the central regions of M31. The nuclear star cluster P3 has an age of 200 Myr (Bender et al. 2005) and hence formed at the same time as the events modeled by Block et al. (2006) and Font et al. (2006). Davidge et al. (2006) find a bright object that is a few arcseconds from the nuclear star cluster P3. This source dominates the central light output of M31 at 4.5 μm and appears to be a massive dust-enshrouded AGB star that—based on its luminosity—may have an age of a few hundred Myr. Saglia et al. (2010) find a counterrotating ring of gas in the central regions of M31, which they interpret as the remnant of a merger ∼0.1 Gyr in the past. They suggest that $10^6 M_\odot$ of stars formed in the central parts of M31 following this merger.

The disk of M31 also contains signatures of an event (or events) that disrupted the ISM. The H I disk of M31 is twisted and warped (e.g., Corbelli et al. 2010), and there is a significant non-rotational kinematic component (e.g., Unwin 1983). Yin et al. (2009) model the chemical properties and the distribution of gas and stars in M31 assuming evolution in isolation. The model does not match the observed gas content at large radii or the radial distribution of star-forming activity throughout the galaxy. Yin et al. (2009) attribute these discrepancies to interactions. An alternative is to accept that the star-forming efficiency in M31 varies with radius but stays constant throughout the Galaxy (e.g., Marcon-Uchida et al. 2010).

The location and distribution of star-forming regions in M31 also differ systematically from those in the Galaxy and M33. While star formation in the Galaxy and M33 tends to be distributed along well-defined spiral arms, a large fraction of the star-forming activity in M31 occurs in rings at $R_{GC} = 10$ and 14 kpc (Thilker et al. 2005; Gordon et al. 2006; Barmby et al. 2006), in stellar arcs, and in spiral arm fragments (e.g., discussion in Efremov 2010). Much of the star-forming activity is (and has been for at least the past 100 Myr—Section 6) concentrated in the ring at $R_{GC} = 10$ kpc, which contributes substantially to the total Hα emission from M31 (Devereux et al. 1994). Despite the evidence that the ISM of M31 has been disrupted, the star-forming environment in these rings is probably not too different from that in the Galactic disk. Indeed, giant molecular clouds (GMCs) in M31 fall along the same size versus line width relation as Galactic GMCs (Sheth et al. 2008), indicating a structural kinship.

The depletion timescale of molecular gas indicates that M31 is much less efficient at forming massive stars than M33 (Tabatabaei & Berkhuijsen 2010). The strength of the UV radiation field throughout the M31 disk is only 40% that in the solar neighborhood (Montalto et al. 2009), and the SFR of M31 is roughly one-half that expected for a galaxy of similar mass and morphology that has evolved in isolation (Yin et al. 2009). Williams (2003) infers an SFR of $\sim 1\ M_\odot\ \mathrm{yr}^{-1}$ for M31, based on studies of resolved stars over a 1.4 deg^2 area. Integrated light diagnostics suggest present-day SFRs for M31 of 0.3 (Tabatabaei & Berkhuijsen 2010), 0.4 (Barmby et al. 2006), and 0.6 (Kang et al. 2009) $M_\odot\ \mathrm{yr}^{-1}$. These are lower than the SFR of the Galaxy (e.g., Boissier & Prantzos 1999; Robitaille

& Whitney 2010) and are on par with the much less massive galaxy M33 (Hippelein et al. 2003; Verley et al. 2007, 2009).

1.5. The Present Study

In the present paper, deep MegaCam observations are used to study the locations and photometric properties of bright resolved stars throughout the disk of M31. Massive main-sequence and evolved stars are detected, and these are used to characterize the SFH during the past few hundred Myr and search for signatures of recent interactions. Atmospheric seeing and sky emission restrict the photometric depth that can be achieved with ground-based data sets when compared with space-based observations. However, ground- and space-based observations of nearby galaxies provide complementary information because they usually sample very different spatial scales. The spatial coverage of space-based data sets of M31 at visible and near-infrared wavelengths tends to be limited. The most extensive such data set is that discussed by Dalcanton et al. (2011), which is restricted to the northeast quadrant of the galaxy. In contrast, our MegaCam data cover almost the entire star-forming disk of M31 out to major axis distances in excess of 30 kpc (>5 scale lengths). Such comprehensive spatial coverage is of interest since the SFH can vary with location over large spatial scales in disks (e.g., Davidge 2010; Davidge & Puzia 2011). Spatial variations of this nature can complicate efforts (1) to determine a representative global SFH if only part of the disk is sampled and (2) to assess the large-scale radial trends that are probes of galaxy evolution.

Two important considerations are the distance to M31 and the reddening model. An absolute distance modulus $\mu_0 = 24.36$, computed by Vilardell et al. (2010) from two double-lined spectroscopic eclipsing binaries, is adopted for this study. Such systems are primary distance indicators (de Vaucouleurs 1978) that rely on geometric parameters directly measured from the application of basic physics. Distances measured with these objects should be less susceptible to calibration uncertainties than those computed from secondary distance indicators. The distance modulus adopted here is in excellent agreement with that computed from Cepheids by Riess et al. (2012).

The baseline reddening model consists of a linear combination of foreground ($A_B = 0.27$; Schlegel et al. 1998) and internal ($A_B = 0.61$; Pierce & Tully 1992) components. The total extinction is thus $A_B = 0.88$ mag. This corresponds to $A_{u'} = 1.05$, $A_{g'} = 0.77$, and $A_{r'} = 0.56$ mag based on the relations listed in Table 6 of Schlegel et al. (1998). It is demonstrated in Section 4 that this total extinction holds for a "typical" main-sequence star in our sample. Of course, the reddening toward any given object depends on factors such as its age, location, and evolutionary state (e.g., Massey et al. 2009), and it is not surprising that there is a substantial spread in extinction throughout the M31 disk. For example, Hodge et al. (2010) find a dispersion of ± 0.23 mag in $E(B-V)$ measurements among young clusters. There is almost certainly an environmental component, as Hodge et al. (2010) and Perina et al. (2010) find $E(B-V) = 0.28$ ($A_{g'} = 1.06$) for young star clusters, whereas Massey et al. (2007) measure $E(B-V) = 0.13$ ($A_{g'} = 0.49$) for young field stars in the M31 disk.

The paper is structured as follows. The observations and the reduction of the data are discussed in Section 2, while details of the photometric measurements, including their calibration and characterization, are discussed in Section 3. Color–magnitude diagrams (CMDs) are presented in Section 4, while the SFH of the M31 disk is investigated in Section 5 using the luminosity functions (LFs) of main-sequence stars. The spatial distribution of main-sequence and evolved stars is examined in Section 6. The paper closes with a summary and discussion of the results in Section 7.

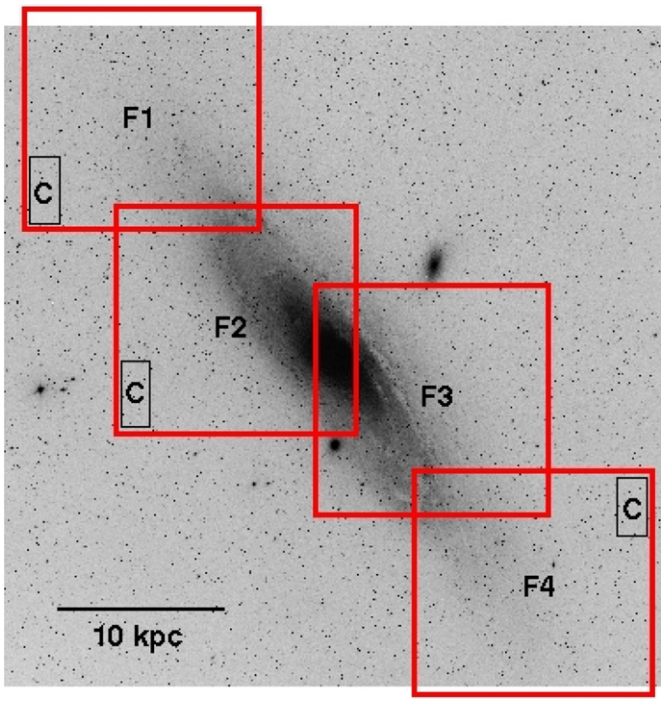

Figure 1. Locations of the four MegaCam fields. The reference image is from the DSS and is in the *E* band. North is at the top, and east is to the left. Each MegaCam field covers roughly ~1 deg^2. The locations of the three control fields that are used to estimate contamination from foreground and background objects are also indicated.

(A color version of this figure is available in the online journal.)

2. OBSERVATIONS AND REDUCTIONS

The data were recorded on the 3.6 m Canada–France–Hawaii Telescope (CFHT) as part of the 2010B MegaCam (Boulade et al. 2003) observing queue. The detector in MegaCam is a mosaic of thirty-six 2048×4612 E2V CCDs. These are deployed in a 4×9 format and cover roughly 1 deg^2 exposure^{-1} with 0.185 arcsec pixel^{-1}.

Four fields that cover almost all of the star-forming disk of M31 were imaged through u^*, g', and r' filters.[8] The locations of the MegaCam pointings are shown in Figure 1. The observations for each field were obtained during a single continuous block of time that typically spanned 2 hr. While archival g' and r' MegaCam data were available of the disk of M31, images in these filters were still recorded for our program to secure a set of single-epoch measurements and thereby suppress scatter in colors that might arise from photometric variability over timescales $\geqslant$2 hr. A log of the observations, showing dates of observations and exposure times for each field, is shown in Table 1. The u^* images have markedly longer exposure times than the g' and r' images because of the comparatively low system throughput at shorter wavelengths.

Initial processing of the data was done with the CFHT ELIXIR pipeline, and this included bias subtraction and flat-fielding. Each pipeline-processed image was divided into

[8] The filter transmission curves can be found at http://www.cfht.hawaii.edu/Instruments/Filters/megaprime.html.

Table 1
Log of Observations

Field No.	Date Observed	Exposure Times (s)
1	2010 Sept 13	$9 \times 600(u*)$
		$4 \times 200(g')$
		$4 \times 200(r')$
2	2010 Oct 31	$6 \times 600(u*)$
		$4 \times 200(g')$
		$4 \times 200(r')$
3	2010 Nov 1	$6 \times 600(u*)$
		$4 \times 200(g')$
		$4 \times 200(r')$
4	2010 Oct 30	$9 \times 600(u*)$
		$4 \times 200(g')$
		$4 \times 200(r')$

six 2×3 CCD sub-mosaics to produce data sets of a manageable size for subsequent processing and photometric analysis. Sub-mosaic images were spatially registered to correct for offsets introduced during acquisition, and the results were stacked according to field and filter.

The MegaCam optics produce modest chromatic distortions across the imaged field, which manifest as location-dependent offsets between the centroids of stars imaged in different filters. The offsets between u^* and g' images taken at moderate airmass and aligned near the optical axis of the instrument can be up to an arcsecond near the edge of the MegaCam science field. To correct for these, the u^* and r' data were mapped into the g' reference frame using the IRAF GEOMAP/GEOTRAN tasks. Stars in the final distortion-corrected images typically have FWHM = 0.7–0.9 arcsec.

3. PHOTOMETRIC MEASUREMENTS AND CHARACTERIZATION

3.1. Basic Methodology

Photometric measurements were made with the point-spread function (PSF) fitting program ALLSTAR (Stetson & Harris 1988). Each PSF was constructed from between 50 and 100 bright, unsaturated stars using routines in the DAOPHOT package (Stetson 1987). In addition to brightness, PSF stars were selected using star-like appearance and the absence of bright neighbors as criteria. Faint companions were subtracted from the wings of PSF stars in an iterative manner, using progressively improved PSFs.

Following the procedure described by Davidge (2010), the raw photometric catalogs produced by ALLSTAR were culled of extended and very faint sources using the error in magnitude that is computed by ALLSTAR, ϵ. This quantity measures the quality of the PSF fit but does not take into account other sources of error, such as those introduced by crowding. While ϵ is only a lower limit to the total uncertainty in source brightness, it provides a means of identifying objects for which photometry may be problematic.

Two rejection criteria were applied. First, all sources with $\epsilon \geqslant 0.3$ mag were deleted. Obtaining meaningful photometric measurements is problematic for objects with such large uncertainties, the majority of which are near the faint limit of the data. Second, point sources define a sequence in the magnitude versus ϵ plane that is narrow at the bright end and fans out toward fainter magnitudes. Objects that are outliers from this trend were removed. This step tends to remove extended sources (e.g., Davidge 2010) and cosmetic defects.

3.2. Calibration

Standard stars are observed during each MegaCam observing block. These observations are used to determine photometric zero points, and the results are placed in MegaCam image headers during ELIXIR processing. We used these header entries to transform instrumental magnitudes into the Sloan Digital Sky Survey $u'g'r'$ system (Fukugita et al. 1996). We note that a comparison of photometric measurements in overlapping sections of fields indicates that the internal field-to-field calibration consistency is a few hundredths of a magnitude.

There are significant differences between the u^* and u' bandpasses, with the central wavelength of u^* falling 200 Å redward of u'. Our u' magnitudes were checked using the UVR measurements of bright stars in M31 published by Massey et al. (2006). The magnitudes from that study were transformed into the Sloan system using equations from Smith et al. (2002), and the results were compared for stars in common with our data set.

The comparisons were restricted to bright stars in uncrowded parts of M31 to suppress the influence of image quality differences between the KPNO and CFHT observations. One consequence of restricting the areal coverage in this way is that the majority of the stars used in the comparison have red colors, as the main body of the star-forming disk (where bright blue stars tend to be found) is intentionally avoided. This caveat notwithstanding, there is excellent agreement between the two sets of measurements, with $\Delta g' = 0.035$ and $\Delta u' = -0.034$, in the sense CFHT–KPNO. The standard deviations about these means are $\sigma_{\Delta g'} = \pm 0.011$ and $\sigma_{\Delta u'} = \pm 0.079$. This agreement is comparable to that found by Davidge & Puzia (2011) in their study of M33.

3.3. Photometric Characterization: Artificial Star Experiments

Sample completeness and uncertainties in the photometry were assessed through artificial star experiments. Artificial stars were assigned magnitudes and colors that hold for main-sequence stars, which are the primary probes of the SFH in this paper. As with observations of real objects on the sky, an artificial star was considered to be recovered only if (1) it was detected in two filters (either $u' + g'$ or $g' + r'$) and (2) it survived the ϵ-based culling criteria described in Section 3.1.

The uncertainties and systematic effects in the photometry that arise due to crowding and/or statistical fluctuations in the noise increase substantially with magnitude when sample completeness drops below 50%. The magnitude at which 50% completeness occurs is thus one estimate of the faint limit. The artificial star experiments indicate that 50% completeness occurs near $u', g' = 25.5$ and $r' = 24.5$ in the outer regions of the disk and $u', g' = 25$ and $r' = 23.8$ at intermediate radii along the major axis. These values are roughly consistent with the observed faint limits of the CMDs (Section 4).

3.4. Photometric Characterization: Image Stacking Experiments

The impact of crowding on photometry can be investigated by stacking images to simulate higher stellar densities (e.g., Davidge 2001b). A shortcoming is that foreground stars and background galaxies, which are more or less uniformly distributed on the sky over angular scales of a few degrees, are

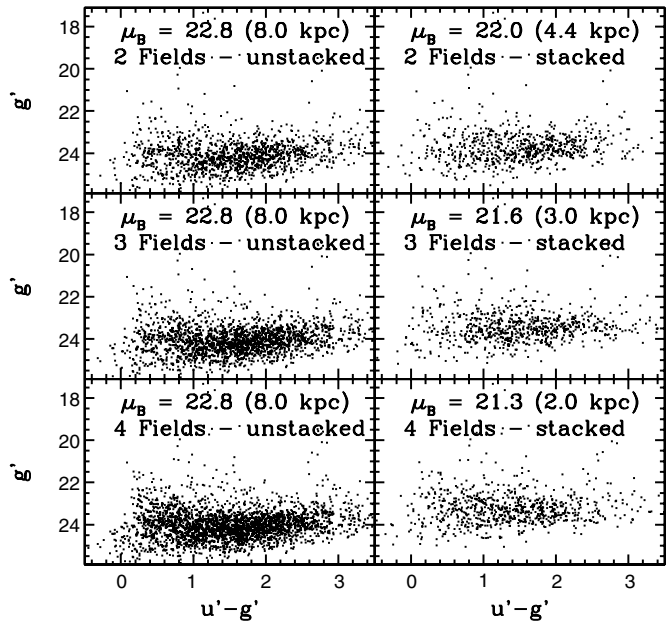

Figure 2. Results of image stacking experiments for $u' + g'$. The left-hand column shows the $(g', u' - g')$ CMDs of two (top row), three (middle row), and four (bottom row) 500 × 500 pixel^2 regions in Field 1. The right-hand column shows the CMDs that are obtained after images of these same regions are stacked to simulate areas of higher stellar density. A comparison of the CMDs in the two columns allows the impact of crowding on the photometry to be assessed. Not surprisingly, the faint limit of the CMDs rises with increasing stellar density, while sample incompleteness at a given magnitude near the faint limit increases with stellar density. The agreement between the unstacked and stacked CMDs when $g' < 23$ suggests that the photometric properties of the brightest stars are not affected by crowding, even in the inner disk of M31.

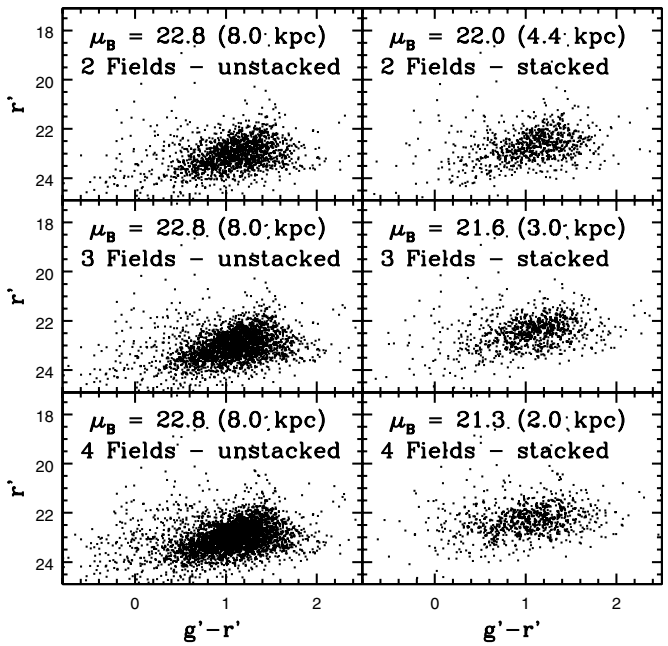

Figure 3. Same as Figure 2, but showing the results of stacking experiments for $g' + r'$. Crowding affects the CMDs when $r' > 22$.

overrepresented in the stacked images. This can be mitigated by selecting fields for stacking that have a moderately high initial stellar density, with the aim of minimizing the number of frames that are co-added to simulate a given stellar density.

Four 500 × 500 pixel^2 areas from Field 1 were selected as the building blocks for the stacking analysis. These are ∼38 arcmin from the center of the galaxy, where the average surface brightness is $\mu_B = 22.8$ mag arcsec^{-2} (Walterbos & Kennicutt 1987). The faint limit of the CMDs in this part of the disk is almost the same as the outermost parts of the disk (Section 4). Two sub-fields were stacked to simulate a field with $\mu_B = 22.0$ mag arcsec^{-2}, while three were combined to simulate $\mu_B = 21.6$ mag arcsec^{-2}. All four sub-fields were combined to simulate $\mu_B = 21.3$ mag arcsec^{-2}.

The magnitudes of stars in the stacked images were measured using the procedures discussed in Section 3.1, and the resulting CMDs are shown in Figures 2 and 3. The left-hand column of each figure shows the CMDs from the unstacked data, while the right-hand column shows the CMDs of the stacked images. The simulated surface brightness of each stacked field is also listed, along with the corresponding major-axis radius from the Walterbos & Kennicutt (1987) light profile.

As expected, crowding elevates the faint limit of the CMDs as one moves to progressively higher surface brightnesses. An interesting practical result is that the photometry of sources with $g' < 23$ and $r' < 22$ appears not to be sensitive to surface brightness in the density regime investigated here. The brightest main-sequence and evolved stars in these data can thus be used to trace the distribution of young stars to within a few kpc of the galaxy center.

4. COLOR–MAGNITUDE DIAGRAMS

We divide the M33 disk into six regions to facilitate analysis and subsequent discussion. Two regions are associated with the rings of UV and FIR emission at $R_{GC} = 10$ and 14 kpc, and these will be referred to as Ring 10 and Ring 14. The Inner Disk is defined to be the region that is interior to Ring 10. The image stacking experiments in Section 3.4 indicate that crowding is an issue for all but the brightest stars with $R_{GC} \sim 2$ kpc, and so the minimum radius for the Inner Disk is set at $R_{GC} = 3$ kpc. The Inner Disk thus probes a region where the disk light dominates over that of the bulge (e.g., Figure A1 of Tempel et al. 2011). The Middle Disk is located between Ring 10 and 14, while the Outer Disk is external to Ring 14.

The Outer Disk is split into two radial intervals. This is done in part because the outer radius of the M31 disk is not clearly defined. In addition, there is evidence that the properties of star formation in low-density environments may differ from those in the inner regions of disks (Bigiel et al. 2010), while secular processes may play a key role in defining the stellar content at large radii (e.g., Roskar et al. 2008; Sanchez-Blazquez et al. 2009). The outermost regions of disks may then be an environment that is distinct from the inner disk, containing population gradients with physical drivers that differ from those at smaller radii.

4.1. $(g', u' - g')$ CMDs

The $(g', u' - g')$ CMDs of roughly 2.1 million sources in various radial intervals are shown in Figure 4. Hess diagrams are shown in Figure 5 to allow the properties of objects in the faint portions of the CMDs to be examined. The radial distances listed in each panel of Figures 4 and 5 are in the plane of the disk and assume 75° inclination. This inclination produces roughly circular rings when observations of warm dust emission are deprojected to simulate the face-on appearance of M31 (Gordon et al. 2006). While the assumption of a single inclination is an obvious pragmatic choice, it is a simplification given that the gas disk of M31 is warped (e.g., Corbelli et al. 2010). This warping,

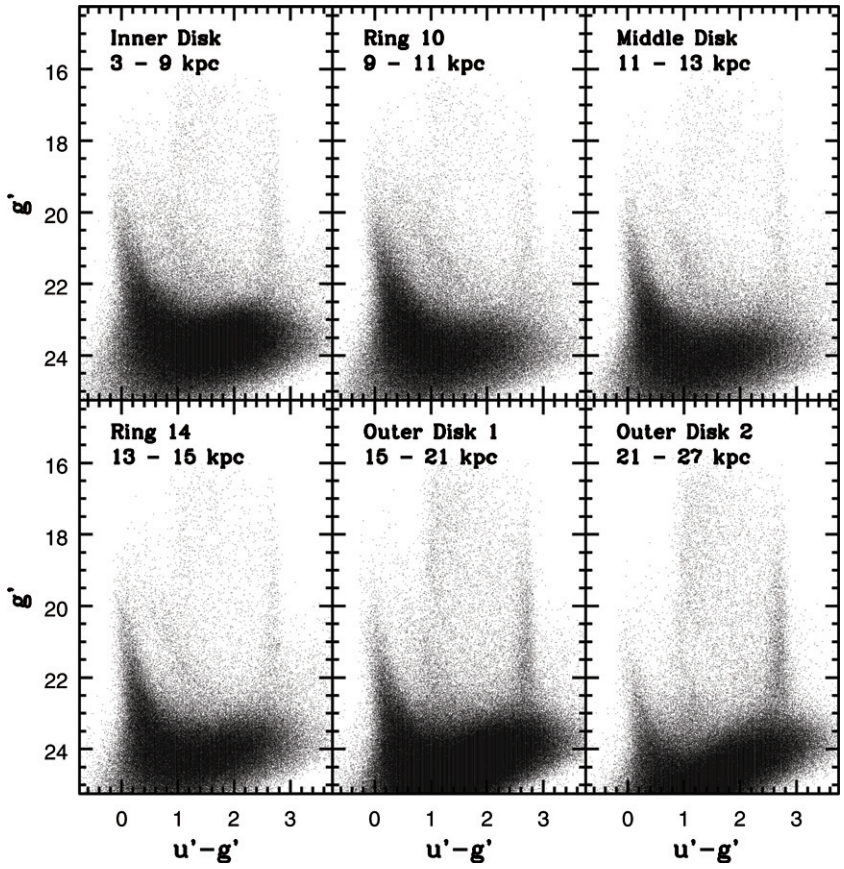

Figure 4. $(g', u' - g')$ CMDs of objects in the disk of M31. The distances in each panel are in the plane of the disk, assuming 75° inclination (Gordon et al. 2006). Main-sequence stars with $g' < 20$ ($M_{g'} < -5$, which have ages <10 Myr) are found out to $R_{GC} \sim 21$ kpc, while fainter main-sequence stars are traced out to even larger radii. Galactic foreground stars form the diffuse sequence with $g' > 16$ and $u' - g'$ between 1 and 3.

coupled with the orientation of M31 on the sky, frustrates efforts to extract clean radial samples that are free of annulus-to-annulus contamination.

Young main-sequence (YMS) stars form a prominent plume in the CMDs, with $u' - g' \sim 0$ at the bright end and $u' - g' \sim 0.5$ near the faint end. Bright blue stars are not restricted to Ring 10 and Ring 14 and are seen in all CMDs with $R_{GC} < 21$ kpc. Recent star formation has thus not been restricted exclusively to Ring 10 and Ring 14. Many of the blue objects with $g' < 18$ ($M_{g'} \leqslant -7$) are bright blue supergiants (BSGs), although some of these may be young compact star clusters. The diffuse sequence of objects that is displaced ~0.6 mag in $u' - g'$ redward of the main sequence, and is most pronounced in the Inner Disk, Ring 10, and Middle Disk CMDs with g' between 20 and 22, is due to helium-burning stars that are at the blue extrema of their evolution. This same feature is seen in Figure 2 of McQuinn et al. (2011).

While the primary probe of evolved stars in our data is the $(r', g' - r')$ CMD (Section 4.2), evolved red stars are also present in the $(g', u' - g')$ CMDs. A population of red objects with $u' - g > 1$ and $g' > 23$ is seen in the Hess diagram of the Inner Disk region in Figure 5. Isochrones (see below) indicate that evolved stars with ages of ~0.2 Gyr pass through this part of the $(g', u' - g')$ CMD. That these red sources occur in large numbers in the Inner Disk $(g' - u' - g')$ CMD when compared with the Ring 10 and the Middle Disk CMDs suggests that the SFR in the Inner Disk was elevated with respect to regions of M31 at larger radii within the past 200 Myr (Section 6).

Background galaxies contribute significantly to the source counts near the faint limit of these data. The majority of background objects have red colors and populate the jumble of red sources with $g' > 23$ that is most obvious in the Outer Disk CMDs. Not all background objects have red colors, and Davidge & Puzia (2011) found that a significant fraction of the objects with blue colors at large radii in M33 are star-forming regions in moderately distant background galaxies. This being said, source counts in areas where the number of M31 disk stars is expected to be small indicate that many of the blue objects with $g' > 20$ in the Outer Disk 2 CMD are bona fide main-sequence stars in M31.

M31 is viewed at intermediate Galactic latitudes, and foreground stars dominate the diffuse spray of objects with $g' < 22$ and $u' - g'$ between 1 and 3 that becomes more prominent toward larger R_{GC}. The blue edge of this sequence is defined by the MSTO of stars in the outer disk and halo of the Galaxy, while the red envelope reflects the properties of low-mass main-sequence stars. Not all of the sources with $u' - g'$ between 1 and 3 are in the foreground, and BSGs with $u' - g' < 2$ and $g' < 22$ (i.e., to the immediate right of the M31 main sequence) are evident in the CMDs of sources with $R_{GC} < 15$ kpc.

The $(g', u' - g')$ CMDs of sources in Ring 10 and Ring 14 are compared with solar metallicity isochrones from Girardi et al. (2004) in Figure 6. Metallicity gradients are present in many spiral galaxies, and so a comparison with isochrones having only one metallicity may seem suspect. However, the metallicities of BSGs in M31 with R_{GC} between 5 and 12 kpc do not vary with radius (Trundle et al. 2002), suggesting that the ISM of

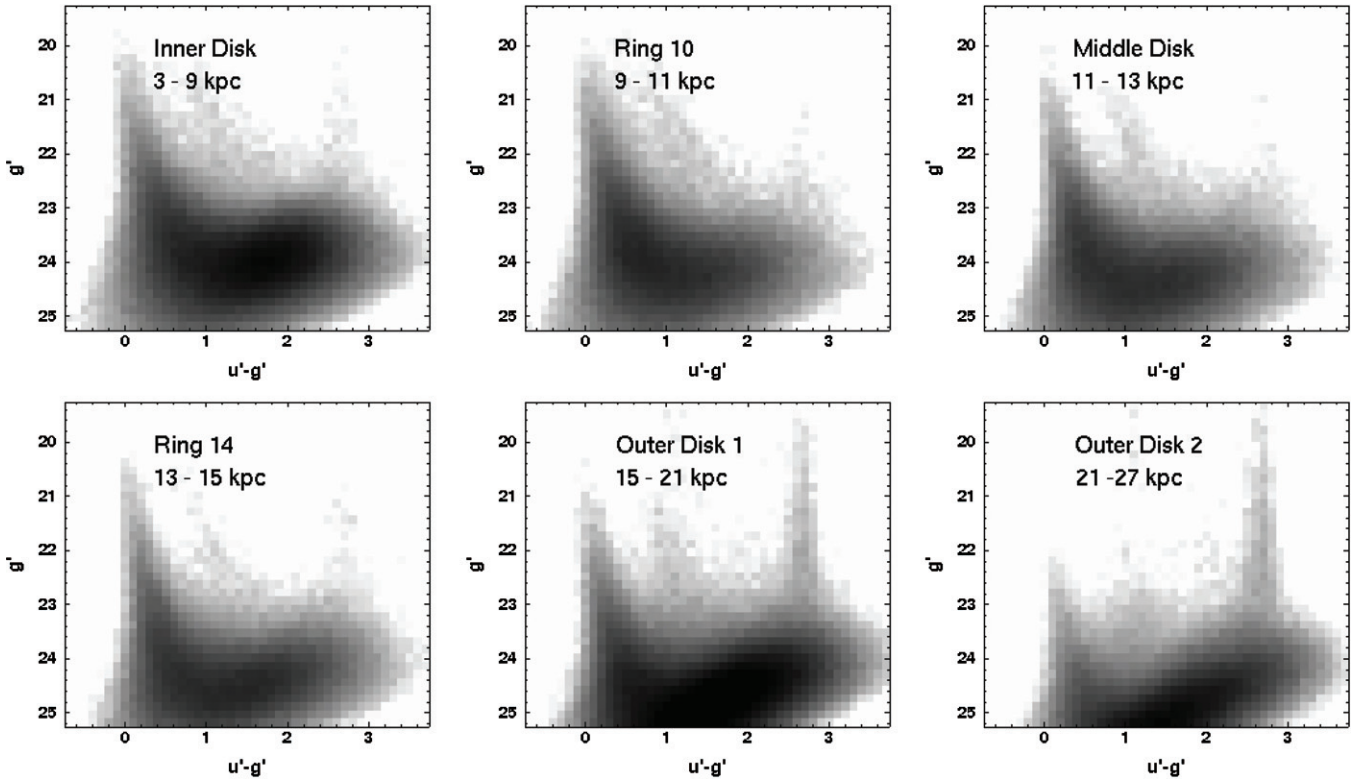

Figure 5. Hess diagrams of the $(g', u' - g')$ CMDs. Binning factors of 0.1 mag in $u' - g'$ and 0.15 mag in g' have been employed, and the aspect ratio is the same as for the CMDs in Figure 4. There is a prominent collection of objects with $u' - g' \geqslant 1$ and $g' > 23$ in the Inner Disk Hess diagram, which is attributed to enhanced star-forming activity in this part of M31 100–200 Myr in the past (Section 6). The Inner Disk aside, there is a tendency for the faint red tongue of objects with $u' - g' > 1$ to become more pronounced as R_{GC} increases. This is due—at least in part—to increased contamination from background galaxies in the diffuse outer regions of the disk.

M31 is well mixed and that the metallicity gradient among moderately young stars is modest. Therefore, with the exception of a single $Z = 0.004$ sequence to demonstrate metallicity effects, the comparisons with isochrones are restricted to a single metallicity.

The image stacking experiments discussed in Section 3 indicate that crowding does not affect greatly the photometric properties of objects with $M'_g < -2$, the majority of which are main-sequence stars with ages <100 Myr. It is thus significant that the zero-age main sequence (ZAMS) defined by the isochrones falls along the blue envelope of main-sequence stars, while the terminal-age main sequence (TAMS), defined by the red extent of main-sequence evolution, follows the red envelope of the blue plume. That the observed blue plume is bracketed by these two evolutionary phases suggests that age is the dominant driver of main-sequence width in our data, rather than photometric errors or differential reddening.

Ring 10 and Ring 14 both contain very young stars. The brightest blue objects in Ring 10 and Ring 14 fall more or less along the 5 Myr isochrone in Figure 6. This is not unexpected given that these annuli are known to contain areas of very recent star formation. It is also evident from the isochrones that the part of the CMD with $M_{g'} > -2$ and $u' - g' > 1$ contains evolved stars with ages $\geqslant$0.2 Gyr. Hence, the red concentration of objects near the faint limit of the $(g', u' - g')$ CMD contains intermediate-age stars.

The blue core helium-burning (BHeB) sequence in M31 is not well matched by the locus of blue loops in the $Z = 0.019$ isochrones, in the sense that the locus of blue loops during supergiant evolution is almost 1 mag in $u' - g'$ redward of the observed sequence. McQuinn et al. (2011) also found differences between the observed and predicted colors of the BHeB sequence in their sample of dwarf galaxies. Such disagreements with observations may be due to—for example—errors in the physics used to generate the models, uncertainties in circumstellar extinction, or uncertainties in the metallicities adopted for the stars. An interesting result from Figure 4 of McQuinn et al. (2011) is that the colors predicted for BHeB stars do not change greatly with metallicity when $Z < 0.019$. The blue loop of the $Z = 0.004$ isochrone in Figure 6 overlaps the M31 BHeB sequence, and one *possible* explanation for the poor agreement between the observed and predicted color of the BHeB sequence in Figure 6 is that the stars in M31 have a metallicity that is no more than one-half solar (i.e., [M/H] ~ -0.3). However, we reiterate that metallicity is just one of the factors that may affect the color predicted for the BHeB sequence.

The comparisons in Figure 6 assume the same reddening for each star. Reddening maps have been constructed for M31 using the distribution of warm and cool dust, and these could be used to estimate reddening for individual sources. However, our MegaCam data are not consistent with the radial extinction trends predicted from dust emission. This is demonstrated in Table 2, where the mean $u' - g'$ color, $\overline{u' - g'}$, of sources with g' between 21.75 and 22.25 is given for five radial intervals. An iterative 2.5σ rejection filter was applied to suppress outliers. The standard deviation about the mean, $\sigma_{u'-g'}$, is also shown, along with the mean optical depth at each R_{GC}, $\tau_{g'}$, taken from Figure 4 of Tempel et al. (2011).

The entries in Table 2 indicate that the plume containing main-sequence stars and BSGs has a dispersion $\pm$0.15 mag at

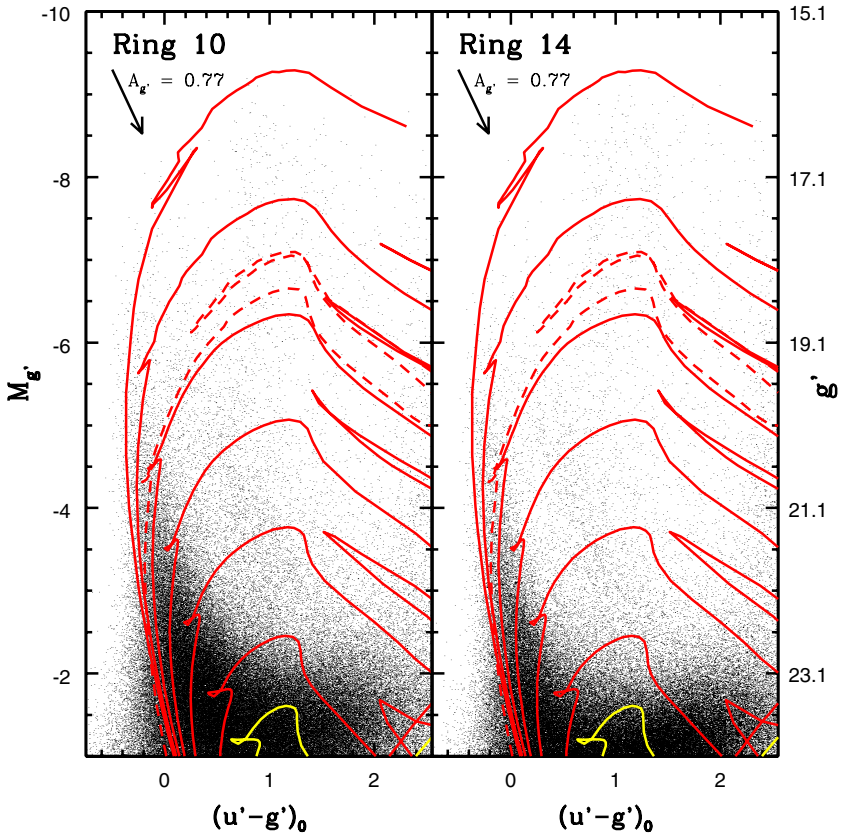

Figure 6. ($M_{g'}, u' - g'$) CMDs of Ring 10 and Ring 14 are compared with $Z = 0.019$ isochrones from Girardi et al. (2004). A reddening vector, with a length that corresponds to the reddening correction applied in this study, is also shown. The red lines are models with ages 5, 10, 20, 40, 80, and 160 Myr, while the yellow line is a 240 Myr isochrone. The dashed red line is a 20 Myr $Z = 0.004$ isochrone, which is included to demonstrate metallicity effects. The theoretical ZAMS falls along the blue envelope of the observed main sequence, while the locus of TAMS points tracks the red envelope. Given that the dispersion due to photometric errors is modest (± 0.07 mag at $M'_g = -2$), the agreement with the modeled ZAMS and TAMS suggests that the width of the main sequence in our data is defined primarily by the ages of stars in our fields, rather than by binarity or differential reddening. It is also evident that the faint red end of the CMD contains evolved stars with ages $\geqslant$0.2 Gyr that are moving from the main sequence to the AGB.

(A color version of this figure is available in the online journal.)

Table 2
Photometric Properties of the Blue Plume near $g' = 22$

R_{GC}	$\overline{u' - g'}$	$\sigma_{u'-g'}$	$\tau_{g'}$
6 kpc	0.380 ± 0.003	± 0.151	0.6
8 kpc	0.384 ± 0.002	± 0.151	0.6
10 kpc	0.378 ± 0.001	± 0.154	1.0
12 kpc	0.377 ± 0.002	± 0.140	0.8
14 kpc	0.383 ± 0.002	± 0.144	0.4

$g' = 22$, supporting the notion that photometric errors make only a modest contribution to the width of the main sequence. The entries in Table 2 further indicate that neither the mean color of the main sequence nor the dispersion about the mean changes significantly with radius between $R_{GC} = 5$ kpc and 15 kpc. Indeed, the mean $u' - g'$ color of the main sequence in this large range of R_{GC} varies by only a few millimagnitudes. To be sure, there are area-to-area variations in extinction within each annulus. However, the radial consistency of the mean $u' - g'$ color indicates that these variations average out to a remarkable degree when stellar measurements are combined azimuthally.

The uniform color of the main-sequence ridgeline in Table 2 is contrary to what might be expected based on the optical depth measurements from Tempel et al. (2011), which predict systematic radial variations in total extinction, with $\tau_{g'}$ peaking in Ring 10. Such an inconsistency would occur if the radial $\tau_{g'}$ measurements obtained from dust emission do not apply to the majority of stars in each angular resolution element. Indeed, a core assumption made by Tempel et al. (2011) is that cool dust is uniformly distributed. There almost certainly *is* a uniformly distributed cool dust component throughout the M31 disk; however, there are also areas of cool dust emission that are concentrated on scales that are smaller than the angular resolution of the facilities that have probed FIR emission, and such a component will skew τ measurements.

The Tempel et al. (2011) optical depth measurements are based on data from the *Spitzer* telescope, the angular resolution of which is roughly 40 arcsec, or $\sim$0.15 kpc in M31, at 160 μm. Each resolution element then has a spatial extent that is roughly one order of magnitude larger than that of a typical GMC. If a significant part of the cool dust emission within a resolution element originates from GMCs, then the extinction of objects that are exterior to the GMCs, but still within the same observed angular resolution element, will be overestimated. The stars that are obscured in GMCs by the cool dust may even be so heavily extincted that they are not detected at visible wavelengths, and if this is the case, then the dust and observed stars are spatially de-coupled. In summary, if there is a cool dust component in M31 that is concentrated on GMC-like spatial scales, then the stars within at least some *Spitzer* resolution elements will not

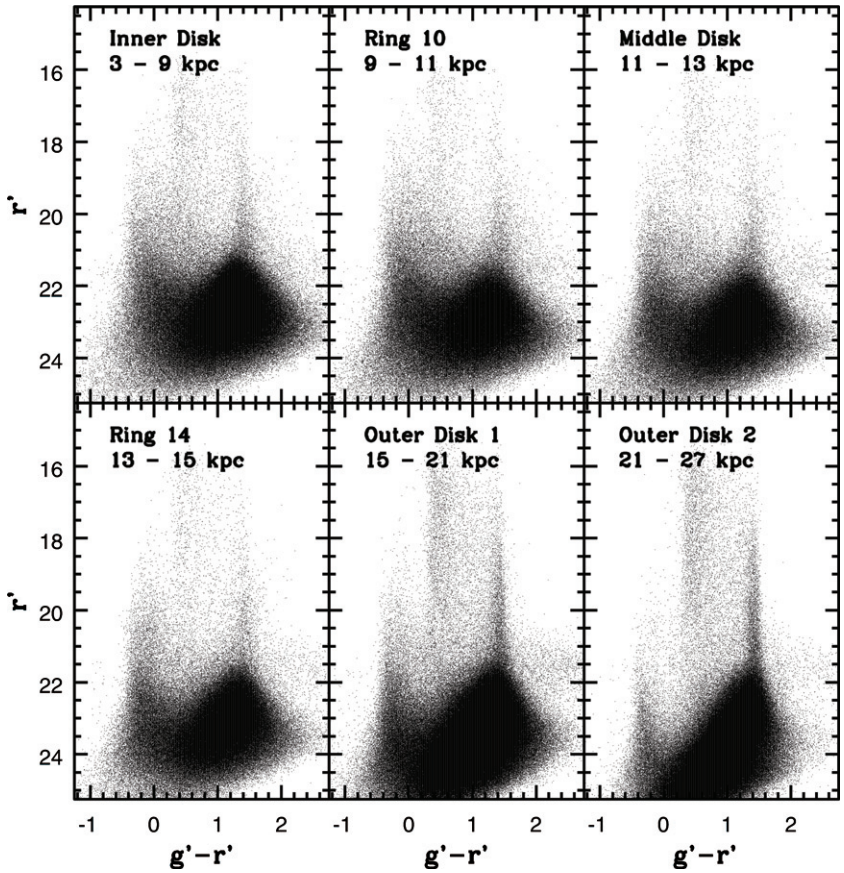

Figure 7. Same as Figure 4, but showing $(r', g' - r')$ CMDs. The plume of objects with $g' - r' < 0$ is a mix of main-sequence stars and BSGs, while RHeB stars dominate the collection of objects with $r' > 21$ and $g' - r'$ between 0 and 2.

be subject to the level of dust extinction that is predicted from dust emission.

4.2. $(r', g' - r')$ CMDs

The $(r', g' - r')$ CMDs of roughly 3.6 million sources in the M31 disk are shown in Figure 7, while the corresponding Hess diagrams are shown in Figure 8. Foreground stars form a spray of objects at the bright end of the CMDs in Figure 7 that has a well-defined blue and red cutoff; this sequence falls between $g' - r' = 0$ and 2 and is most obvious when $r' < 21$. There is also a prominent blue plume with $g' - r' \sim -0.1$ that contains main-sequence stars. The blue plume is less well defined in the $(r', g' - r')$ CMDs than in the $(g', u' - g')$ CMDs, and it is demonstrated below that this is probably a consequence of the trajectories followed by stars on this CMD as they evolve off of the ZAMS.

A collection of objects with $r' > 22$ and $g' - r'$ between 0 and 2 forms a prominent feature in the $(r', g' - r')$ CMDs. At small and intermediate R_{GC} this part of the CMD is dominated by a mix of red core helium-burning (RHeB) giants/supergiants and stars that are evolving on the AGB. Background galaxies make a progressively larger contribution to the faint red end of the CMDs as one moves to larger R_{GC}.

The $(r', g' - r')$ CMDs of Ring 10 and Ring 14 are compared with solar metallicity isochrones from Girardi et al. (2004) in Figure 9. The isochrones follow a near-vertical trajectory on the $(r', g' - r')$ CMD after leaving the ZAMS; this continues past the TAMS until the onset of red loops, smearing the main sequence in a vertical direction on the CMDs, and making the blue plume in the $(r', g' - r')$ CMD near $g' - r' \sim -0.1$ more diffuse than in the $(g', u' - g')$ CMD. It is encouraging that the blue plume in the $(r', g' - r')$ CMDs is bracketed by the ZAMS and the inflexion points in the isochrones that mark the onset of red loops.

The isochrones indicate that the red jumble is made up of stars in a mix of evolutionary stages, some of which are RHeB and others evolving on the AGB. Given that the timescale for core helium burning is much longer than the timescale to evolve on the AGB, stars in the former stage of evolution are the dominant population. The 160 and 240 Myr isochrones pass through the main concentration of red sources that have $M_{r'} > -3$, indicating that the majority of these stars have progenitor masses $\sim$3–4 $M_{\odot}$.

Line blanketing affects the photometric properties of very red evolved stars at visible and red wavelengths, causing the most luminous portions of the AGB at moderate and higher metallicities to bow over on the $(r', g' - r')$ CMDs (e.g., Bica et al. 1991). This is evident in Figure 9, as the 160 Myr isochrone plunges to fainter $M_{r'}$ when $(g' - r') > 1.5$. The most luminous portions of the AGB are almost certainly missing from these CMDs, and so identifying the AGB-tip is problematic.

4.3. The $g' - r'$ Color Distribution

The color distributions of stars can be used to investigate field-to-field variations in the recent SFH in a purely empirical manner. The $g' - r'$ histogram distributions of sources in three R_{GC} intervals with $M_{r'}$ between -4 and -3, which corresponds to r' between 20.9 and 21.9 based on the apparent r'

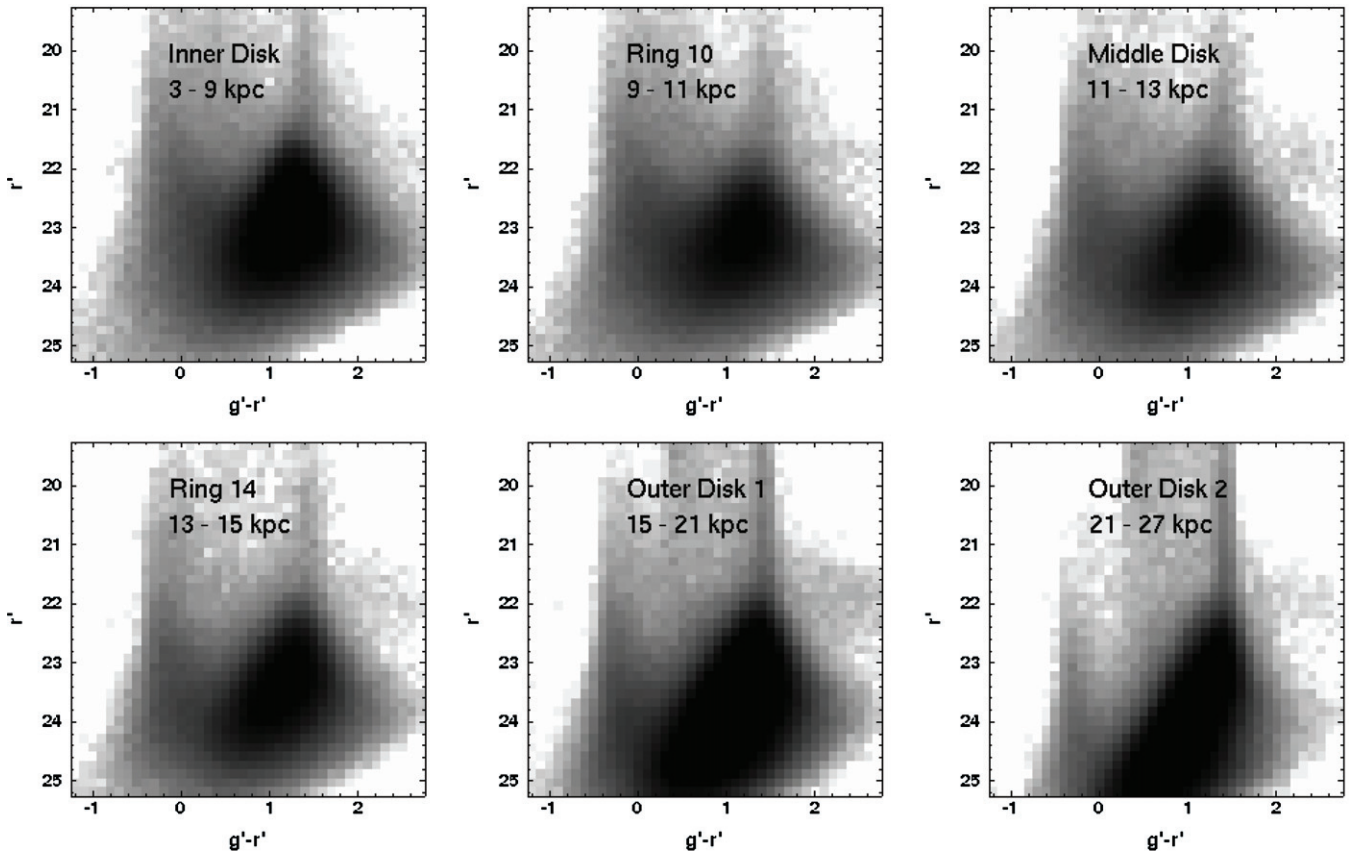

Figure 8. Hess diagrams of the $(r', g' - r')$ CMDs. A 0.1 mag binning is employed in $g' - r'$, while 0.15 mag binning has been employed in r'. The aspect ratio is the same as the CMDs in Figure 7. There is a prominent red sequence with $g' - r' \geqslant 0.5$ and $r' > 22$ in the Inner Disk, which is made up of RHeB and AGB stars and is attributed to enhanced star-forming activity in this part of M31 during intermediate epochs (Section 6). Contamination from background galaxies becomes more important in this red sequence toward larger R_{GC}.

distance modulus, are compared in Figure 10. Comparisons with isochrones in Figure 9 indicate that the blue peak is populated by stars with ages <100 Myr, while the red peak contains stars with ages between 60 and 200 Myr.

The number counts in each radial interval have been corrected statistically for foreground and background contamination using source counts in areas that are external to Outer Disk 2. These control fields, the location of which are indicated in Figure 1, were examined by eye to ensure that they do not contain obvious concentrations of young stars. The control fields almost certainly contain some intermediate-age stars that belong to M31, and so the number counts in these areas may (slightly) overestimate the level of foreground and background contamination at the faint end.

That Ring 10 has been an area of star-forming activity during the past 100 Myr is clearly evident from the number of blue stars in the top panel of Figure 10. The mix of young stars (i.e., those in the blue color peak) to intermediate-age stars (i.e., those in the red color peak) changes with radius, and these variations are explored in the lower panel of Figure 10, where the color distributions have been normalized according to the number of objects with $g' - r'$ between −0.25 and 0.25. There is a wide dispersion in the relative amplitudes of the blue and red peaks. The ratio of red to blue objects in the Inner Disk is substantially larger than in either Ring 10 or the Middle Disk, indicating that the SFH in this part of M31 was skewed to higher levels of activity 60–200 Myr in the past. This is another manifestation of the pronounced red stellar concentrations that are seen in the Hess diagrams of the Inner Disk in Figures 5 and 8. The SFH of the Inner Disk during intermediate epochs is re-visited in Section 6.

The blue sequence in the Middle Disk peaks at a bluer $g' - r'$ color than at smaller radii. A comparatively low reddening for the Middle Disk is probably not driving the peak color of blue stars, as there is not a corresponding shift in the color of the main sequence on the $(g', u' - g')$ CMD (Section 4.1). Rather, the trajectory of the isochrones on the $(r', g' - r')$ plane makes the $g' - r'$ color distribution of blue stars more susceptible to variations in the recent SFH. The blue sequence will narrow as stars at the older end of the ∼100 Myr age range are removed, as these stars have redder colors than younger stars in a given magnitude interval. This may not be accompanied by a skewing of the color distribution of red stars, as these objects span a much larger range of ages than main-sequence stars with the same $M_{r'}$, and so their mean colors are less susceptible to variations in the SFH.

5. MAIN-SEQUENCE STARS AND THE RECENT STAR-FORMING HISTORY

5.1. Main-sequence LFs

As in our study of M33 (Davidge & Puzia 2011), we use the u' LF of blue stars to probe the SFH of the M31 disk. Our u' photometry includes main-sequence stars throughout much of the M31 disk with ages ∼100–200 Myr, allowing the SFH in this time frame to be directly probed. The damping time for large-scale star-forming activity in disks is 10^8–10^9 yr (e.g., Leitherer 2001), and so elevated SFRs may linger for this time

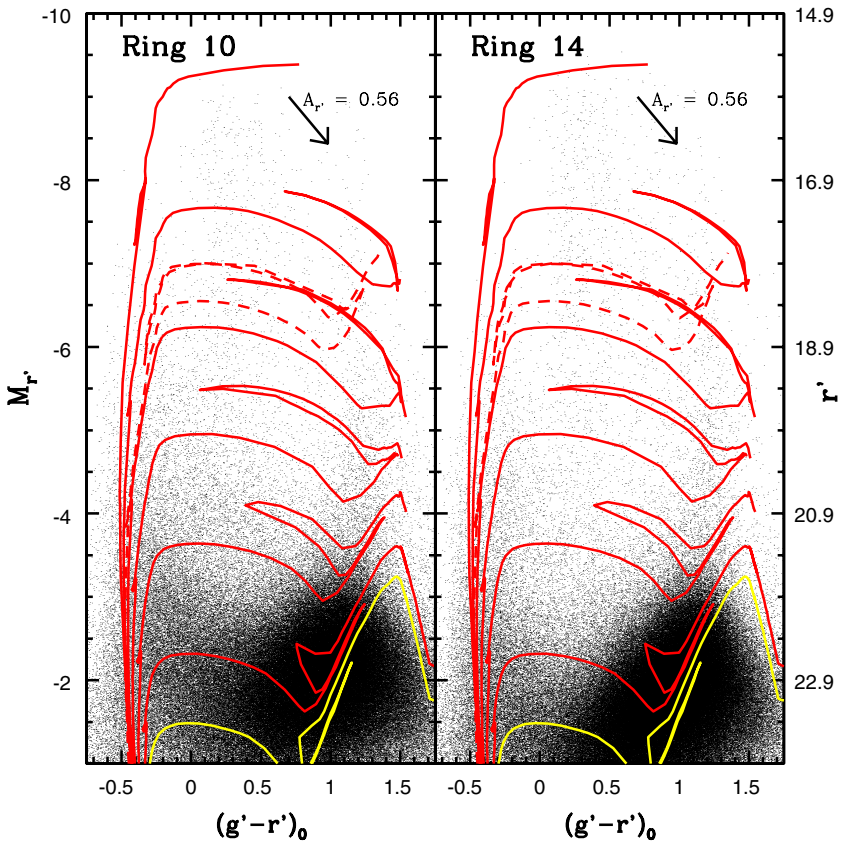

Figure 9. Same as Figure 6, but showing ($M_{r'}$, $g' - r'$) CMDs. The near-vertical trajectory of the isochrones after they leave the ZAMS produces a more diffuse sequence of blue stars than on the (g', $u' - g'$) CMDs. The collection of red objects with $M_{r'} > -3$ is populated by intermediate-mass RHeB stars, AGB stars, and background galaxies.

(A color version of this figure is available in the online journal.)

after they are initiated. Therefore, inferences can be made into the more distant past than would otherwise be permitted from resolved stars.

Following Davidge & Puzia (2011), LFs were constructed of sources with $(u' - g')_0$ between −0.5 and 0.5. The majority of objects in this color range are main-sequence stars. While most foreground and background objects in the CMDs have red colors, there are modest numbers of contaminants that fall within the color interval considered here. These include blue horizontal branch stars in the Galactic halo and star-forming regions in moderately distant spiral galaxies. We account for these statistically using number counts in portions of our MegaCam fields that are offset from the disk of M31 (Section 4.3). The mean LF in these control regions follows a power law, and a characteristic exponent and zero point were determined by using the method of least squares to fit a power law to this LF. This fitted relation was then subtracted from each of the observed LFs, after scaling to account for differences in angular coverage.

The LFs of various radial intervals are compared in Figure 11. The number counts in the top panel are as observed on the sky, and these are given in units of counts arcmin^{-2} per 0.5 mag interval in $M_{u'}$. The ∼1 dex offset between the Middle and Outer Disk LFs is consistent with the Walterbos & Kennicutt (1987) surface brightness profile, as is the 0.5 dex (i.e., 1.25 mag arcsec^{-2}) dispersion between the LFs with R_{GC} in the range 5–15 kpc. This broad consistency between star counts and surface photometry is encouraging and suggests that the bright blue stars detected in the MegaCam data are not affected by crowding.

The LFs in the bottom panel of Figure 11 have been normalized to match the Ring 10 LF between $M_{u'} = -3.75$ and −5.25, thereby allowing the shapes of the LFs to be compared. The LFs follow power laws, and the Outer Disk 2 LF is steeper than the rest. The mix of massive and intermediate-mass stars in the Outer Disk thus differs from that in the Inner Disk.

The LFs of the Inner Disk, Ring 10, and the Middle Disk in the lower panel of Figure 11 are similar. This is perhaps surprising given the concentration of star-forming pockets in Ring 10 (Section 6). However, it should be kept in mind that the LFs are azimuthal averages, and isolated star-forming pockets will only influence the mean LF if they occur in large numbers. In fact, while Ring 10 and Ring 14 contain areas of intense recent star formation, they do not stand out in the UV color profile measured by Thilker et al. (2005); rather, the UV color stays roughly constant between 10 and 15 kpc. The comparisons in Figure 11 indicate that the mix of young to intermediate-age stars in Ring 10 is not different from that in the Inner or Middle Disks—when averaged over large areas, the SFHs of these regions have been broadly similar during the past 100–200 Myr.

5.2. A Comparison with M33

A comparison of the properties of bright main-sequence stars in M31 and M33 provides a purely empirical means of assessing the relative star-forming activities of these galaxies during recent epochs. To be sure, star-forming activity in disk galaxies depends on a number of factors, such as environment and mass, and it would be of interest to compare the stellar content of M31 with that of other large galaxies of similar

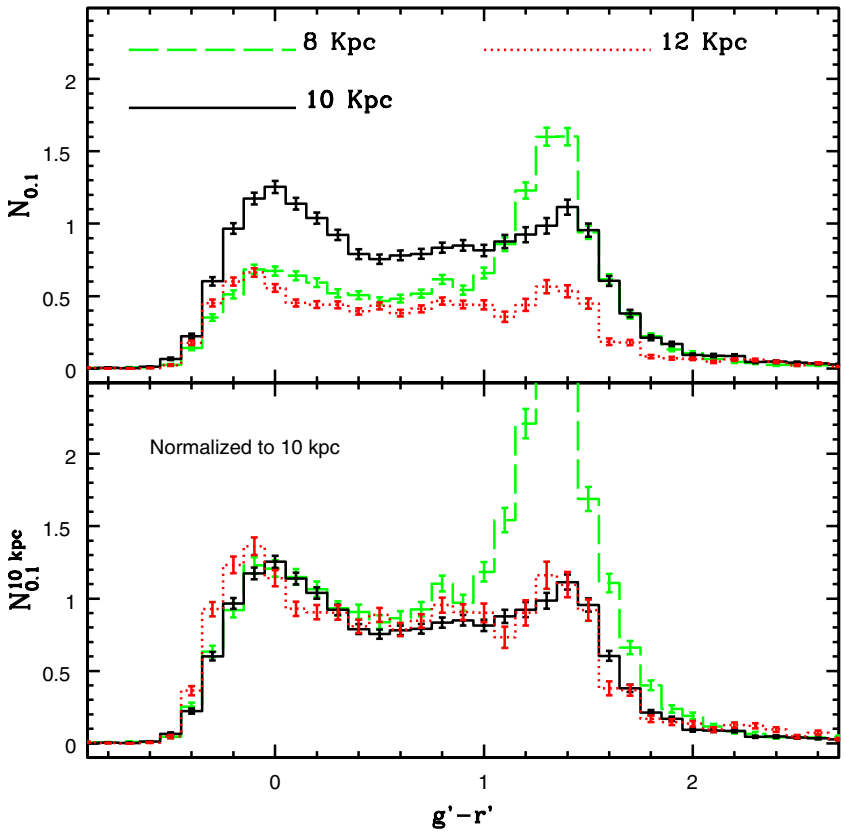

Figure 10. $(g' - r)$ distributions of objects with $M_{r'}$ between –3 and –4 (i.e., r' between 20.9 and 21.9) in three radial intervals. $N_{0.1}$ is the number of objects arcmin^{-2} per 0.1 mag interval in $g' - r'$, corrected for foreground and background objects using the procedure described in the text. The color distributions in the lower panel are the same as those in the top panel and have been normalized to the number of objects with $g' - r'$ between –0.25 and 0.25 (i.e., the approximate color interval of the blue peak). The peak color of the blue plume in the 12 kpc intervals is offset ∼0.1 mag blueward of the peak in the other intervals. Given the radial uniformity of the $u' - g'$ color of the main sequence (Section 4.1), coupled with the path followed by isochrones on the $(r', g' - r')$ plane, we attribute this offset to differences in the SFH within the past ∼0.1 Myr. The 8 kpc interval contains the highest fractional contribution from evolved red stars, indicating that this part of M31 contains a higher fraction of stars that formed 100+ Myr in the past than in the other areas.

(A color version of this figure is available in the online journal.)

morphological type; however, such data do not yet exist. Differences in size and morphological type aside, M33 is an important comparison object as it is at roughly the same distance as M31 and has been the subject of a number of investigations. The SFHs of M31 and M33 have probably also been coupled at some point in the past (Section 1.3). Finally, the specific SFR (sSFR) of M33 is near the midpoint of spiral galaxies in general (Munoz-Mateos et al. 2007), making it a benchmark for activity in a "typical" star-forming galaxy. The M33 MegaCam data set examined by Davidge & Puzia (2011) was recorded during observing conditions that were similar to those of the present M31 observations and are adopted here for comparisons with M31.

Main-sequence stars with ages <10 Myr are traced throughout much of M33 (Davidge & Puzia 2011) and M31 (Section 3), and these stars provide a direct means of comparing the SFRs of these galaxies. Davidge & Puzia (2011) found 3000 massive main-sequence stars and BSGs in M33 with ages ⩽10 Myr. Applying the M33 selection criteria of $M_{u'} \leqslant -5.8$ to the current data, we find that there are 10^3 similar objects in M31. The SFR in M31 during the past 10 Myr has thus been one-third that of M33. For comparison, the integrated Hα luminosities of M31 and M33 are comparable (e.g., Kennicutt et al. 2008), while M31 has a slightly higher FIR flux than M33 (Rice et al. 1988).

The sSFR is a measure of the rate at which stellar mass grows due to star formation. The bulk of the K-band light from most galaxies has its origins in old and intermediate-age stars, and so integrated K-band brightness serves as a crude proxy for total stellar mass. Adopting the apparent K magnitudes of M31 and M33 from Jarrett et al. (2003) and a distance modulus of 24.92 for M33 (Bonanos et al. 2006), the integrated total brightnesses of these galaxies are $M_K = -23.4$ (M31) and $M_K = -20.9$ (M33). Based on the numbers of blue stars with ages ⩽10 Myr (see above) and their integrated K-band brightnesses, the sSFR of M31 is only ∼3% that of M33. The difference between the sSFRs of M31 and M33 is almost certainly greater than this, as it has been assumed that M31 and M33 have identical K-band mass-to-light ratios (M/L_K). In actual fact, given the higher relative fraction of young stars in M33, the M/L_K of M33 is probably lower than that of M31. M/L ratios at a given age depend on metallicity, although for effective ages $\geqslant 10^9$ yr the differences between the M/L ratios predicted by $Z = 0.02$ and $Z = 0.008$ models are minuscule (e.g., Figure 4 of Mouhcine & Lancon 2003). Minor differences in the relative M/L ratios of these galaxies notwithstanding, it is clear that M31 is practically dead in terms of recent star-forming activity when compared with M33.

The M31 and M33 LFs, normalized in the interval $M_{u'} = -4$ to –5, are compared in Figure 12. The M33 LF is that of objects with R_{GC} between 6 and 8 kpc from Davidge & Puzia (2011). The LF of sources in this part of the galaxy is representative of the main body of the M33 disk.

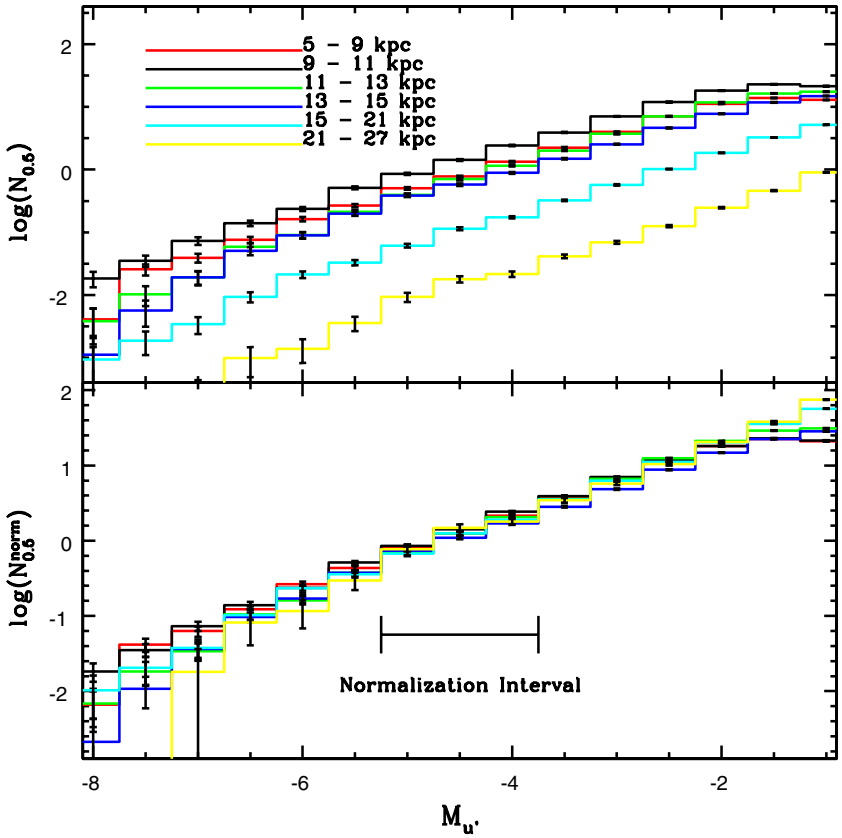

Figure 11. Top panel: the $M_{u'}$ LFs of objects with $(u' - g')_0$ between –0.5 and 0.5, where $N_{0.5}$ is the number of sources arcmin^{-2} per 0.5 mag interval in u'. The LFs have been corrected for foreground and background contamination using the procedure described in the text. Bottom panel: the $M_{u'}$ LFs normalized to the Ring 10 counts between $M_{u'} = -3.75$ and –5.25. The LFs of sources with R_{GC} between 15 and 27 kpc differ from those at smaller radii, indicating that the mix of massive and intermediate-mass stars changes throughout the M31 disk.

(A color version of this figure is available in the online journal.)

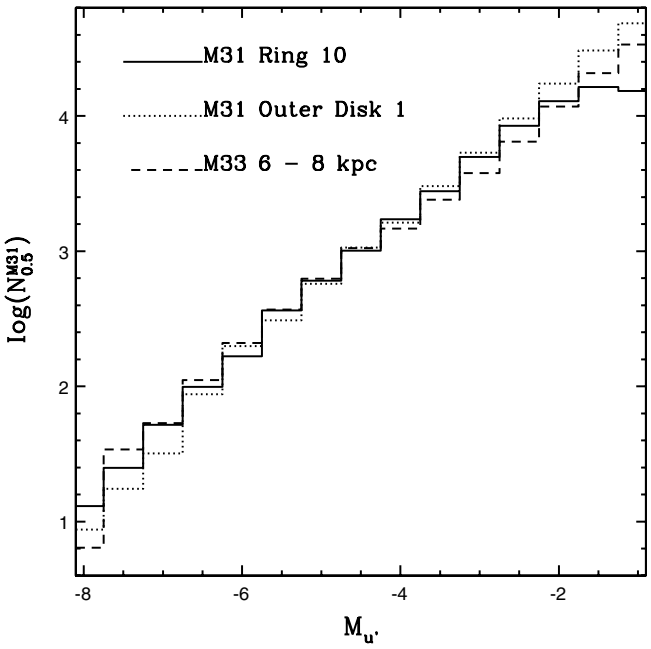

Figure 12. Ring 10 and Outer Disk 1 LFs are compared with the LF of stars in the M33 disk with R_{GC} between 6 and 8 kpc. The LFs have been normalized to match the M31 Ring 10 LF in the $M_{u'}$ interval between –3.75 and –5.25. The M33 LF differs from the M31 LFs, indicating different recent SFHs.

There are conspicuous differences between the M31 and M33 LFs in Figure 12. These differences are likely not a result of differences in metallicity between stars in the disks of M31 and M33. While model LFs of blue sources with $Z = 0.019$ and $Z = 0.008$ do differ, the differences are largely restricted to $M_{u'} < -6$. This magnitude regime is dominated by BSGs, the properties of which are affected by metallicity-dependent mass loss rates. When $M_{u'} > -6$ main-sequence stars dominate, and the model LFs of blue sources show only slight differences.

When compared with the M33 disk, Outer Disk 1 has a lower number of stars with ages of a few tens of Myr with respect to stars that formed a few hundred Myr in the past. When compared with the M31 LFs, the M33 LF is also deficient in stars with $M_{u'}$ between –2 and –4, which is an $M_{u'}$ range that corresponds to MSTO ages of 40–100 Myr. Davidge & Puzia (2011) found that the LF of bright main-sequence stars that formed during the past few hundred Myr in M33 is well matched by a constant SFR (cSFR) model, and the comparisons in Figure 12 indicate that such an SFH does not hold for M31. The SFH of the M31 disk is examined in more detail in the next section.

5.3. Comparisons with Models

We use a forward modeling approach in which model LFs are constructed for pre-defined SFHs and are then compared with the observations. Models were generated from the $Z = 0.019$ Girardi et al. (2004) isochrones using routines in the STARFISH package (Harris & Zaritsky 2001). The models assume an IMF power-law index $\alpha = -2.7$, which Kroupa et al. (1993) find holds for massive stars. Models with a Salpeter (1955) IMF

differ only slightly from those used here (e.g., Figure 11 of Davidge & Puzia 2011).

The u' LF of main-sequence stars provides a relatively robust means of investigating SFHs, as the main sequence is probably the best understood phase of stellar evolution. Still, there is an incomplete understanding of the physical processes that affect the structure and evolution of massive main-sequence stars. These include uncertainties in convection, which is the dominant mode of energy transport in the central regions of massive core hydrogen-burning stars, mass loss, and rotation. While these uncertainties affect the post-ZAMS models of massive stars, it is encouraging that the ZAMS and TAMS loci predicted by the isochrones match the blue and red envelopes of the main sequence on the CMDs (Section 4).

Statistical studies of main-sequence stars are susceptible to uncertainties in the properties of close companions, which are not resolved at the distance of M31. These uncertainties are not an issue for statistical studies of evolved stars, as the light from the most evolved star in a close stellar system swamps that from less evolved companions at visible wavelengths. However, if all the stars in a close system are on the main sequence, then—depending on the mass ratio—companions may contribute a significant fraction of the total system light. While many of the sources in our data are unresolved systems, if the statistical properties of these systems (e.g., the frequency of binary or higher-order systems, the mass ratio of components, etc.) do not change with the mass of the primary, then the main-sequence LF will still yield useful information for a differential examination of the SFH.

The MegaCam data sample stars in a wide range of evolutionary states, all of which provide information about the SFH of M31. However, combining information from different evolutionary states to investigate the SFH may lead to complications when interpreting the results, as the dominant sources of uncertainties in the input model physics vary with evolutionary phase. Comparisons of the SFHs of galaxies at different distances may be most prone to uncertainties related to evolutionary state, as the SFHs may be based on objects in very different stages of evolution. Gogarten et al. (2010) suggest that this may be a factor when comparing the SFHs of M33 and NGC 300. The impact of uncertainties in models of the most advanced stages of stellar evolution on SFHs has been investigated by Melbourne et al. (2010), who compute separate SFHs for a dwarf galaxy using main-sequence stars and AGB stars. The two SFHs differ substantially, and Melbourne et al. (2010) attribute this difference to an incomplete empirical calibration of the AGB models, which rely heavily on the LMC and SMC as benchmarks.

The models used here assume a fixed metallicity and so do not account for metallicity evolution. While the mean metallicity of a disk grows with time as material that is processed in stars is recycled into the ISM, a fixed metallicity is appropriate given that our models cover a time span that is short when compared with the enrichment timescale of a disk. Indeed, the age–metallicity relation of the solar neighborhood during recent epochs has a shallow slope (e.g., Edvardsson et al. 1993), and the rate of metallicity evolution in M31 will be even more subdued than this given the lower SFR.

The most basic SFH model is that of an SSP, in which all stars have the same age and metallicity; SSP LFs are also the building blocks from which LFs that track more elaborate SFHs are constructed. Because galaxies are composite stellar systems, it is unlikely that their LFs will be well matched by SSP models. Still, if a galaxy experiences a single large episode of star formation that is caught early in its evolution, then the LF of the brightest stars may follow that of an SSP.

The u' LFs of main-sequence stars in three radial intervals are compared with a $\log(t_{yr}) = 6.8$ SSP model LF in Figure 13. The Ring 10 LF is similar to that of the Inner and Middle Disk regions (Figure 11), and so comparisons with models are restricted to the four intervals shown in Figure 13. M31 is a composite stellar system, and so it is not surprising that there is poor agreement between the model SSP LF and the observations. Still, the Ring 10 LF, which samples a region with a high concentration of recent star formation, has an exponent that comes closest to matching that of the SSP model.

The SFHs of isolated, passively evolving disks may be affected by stochastic effects, with spikes in star-forming activity due to events such as the passage of spiral arms and the propagation of density waves from supernovae in young clusters and associations. Evidence for variations in the SFH of the solar neighborhood due to the passage of spiral arms has been found by Hernandez et al. (2000). Nevertheless, the impact of stochastic events will average out when considered over long time spans and large areas, and the SFHs of passively evolving disks might be expected to come close to that of a cSFR.

The u' LFs are compared with cSFR models in Figure 14, and there is much better agreement with the observations than in Figure 13. In fact, the cSFR model provides a reasonable match to the Outer Disk 2 LF and is a fair representation of the Outer Disk 1 LF. Still, with the exception of the Outer Disk 2 LF, the cSFR model LFs in Figure 14 tend to be steeper than the observed LFs. Indeed, while the cSFR model is a reasonable match to the Outer Disk 1 observations with $M_{u'} > -5$, which corresponds to MSTO ages $\geqslant$10 Myr, it underestimates the number of stars at the bright end. These differences are even more evident when the Ring 10 and Ring 14 LFs are compared with the cSFR model.

Given the differences between the observations and models in Figure 14, we investigated SFHs in which the SFR during the past 10 Myr has increased with respect to that expected for a cSFR at earlier epochs. Models were generated in which the recent SFR was increased by various amounts, and the results were compared with the observed LFs; the best matches, selected by eye, are shown in Figure 15. Also shown in each panel is b_{100}, which is the ratio of the number of stars that formed within the past 10 Myr to the number that formed in the interval 10–100 Myr. The Outer Disk 2 LF is not shown in Figure 15, as it is represented adequately by the cSFR model.

Models with elevated recent star-forming activity better match the LFs of the three regions shown in Figure 15 than the cSFR models. Higher recent SFRs are required to match the Ring 10 and Ring 14 LFs than is required to match the Outer Disk 1 LF. While this is consistent with Rings 10 and 14 being areas of comparatively intense recent star-forming activity, if elevated levels of recent star formation occur in only part of Outer Disk 1 (i.e., at the smallest R_{GC} in this region), then the effect of any recent increase in the SFR will be diluted. The differences in the amplitude of recent star-forming activity aside, it is clear that the recent upswing in star-forming activity has not been restricted to Ring 10 and 14, but occurred over a large fraction of the disk—the change in the recent SFR is not a localized phenomenon that is restricted to only a small part of the M31 disk, but is more global in nature.

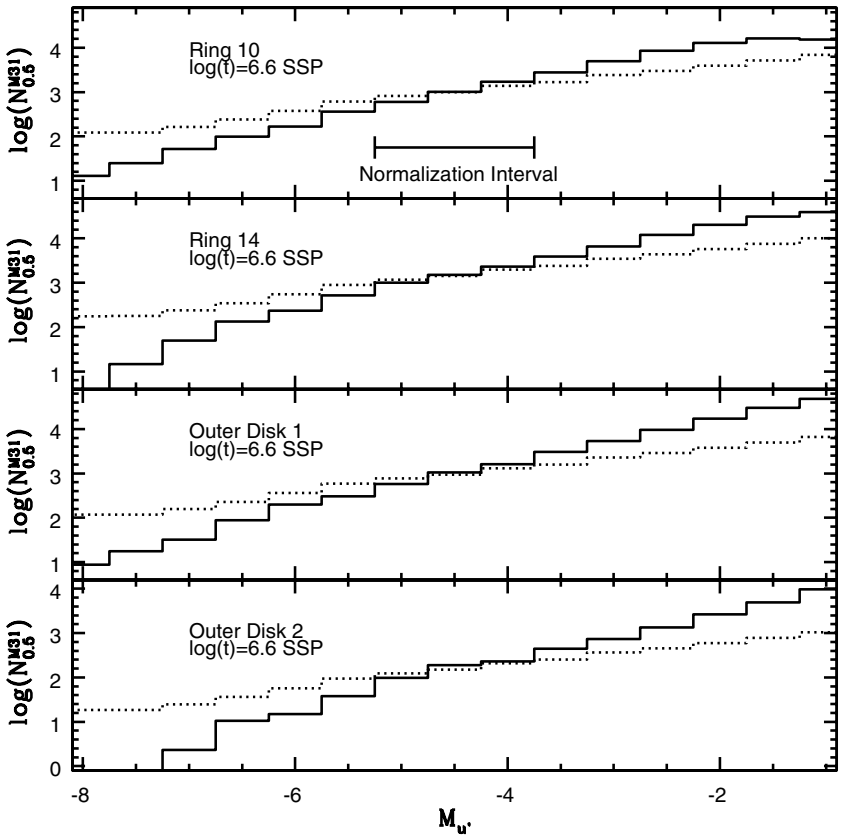

Figure 13. u' LFs of main-sequence stars in four radial intervals (solid lines) are compared with an SSP model LF having $t = 5$ Myr, $Z = 0.019$, and an IMF exponent $\alpha = -2.7$ (dotted lines). The model has been shifted vertically to match the M31 LFs in the interval $M_{u'} = -3.75$ to –5.25. $N_{0.5}^{M31}$ is the number of sources in each interval arcmin^{-2} per 0.5 mag interval in $M_{u'}$. The SSP model is a poor match to the observations.

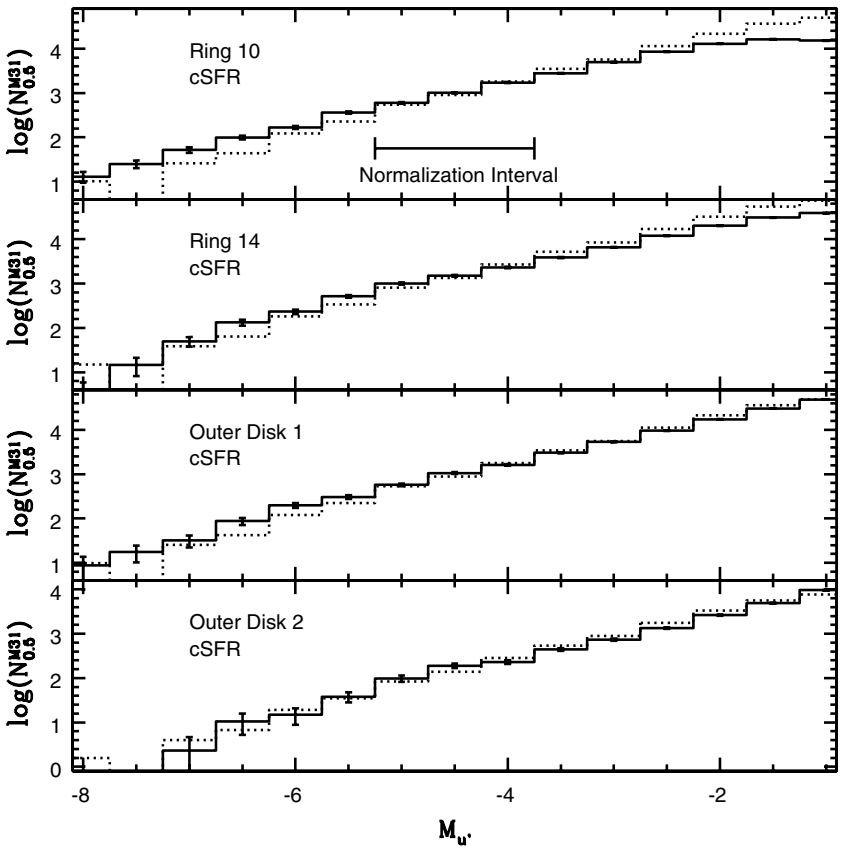

Figure 14. Same as Figure 13, but showing constant SFR (cSFR) models (dotted lines). The cSFR model is a better match to the observations than the SSP model in Figure 13. Still, with the exception of Outer Disk 2, there is a tendency for the models to be steeper than the observed LFs.

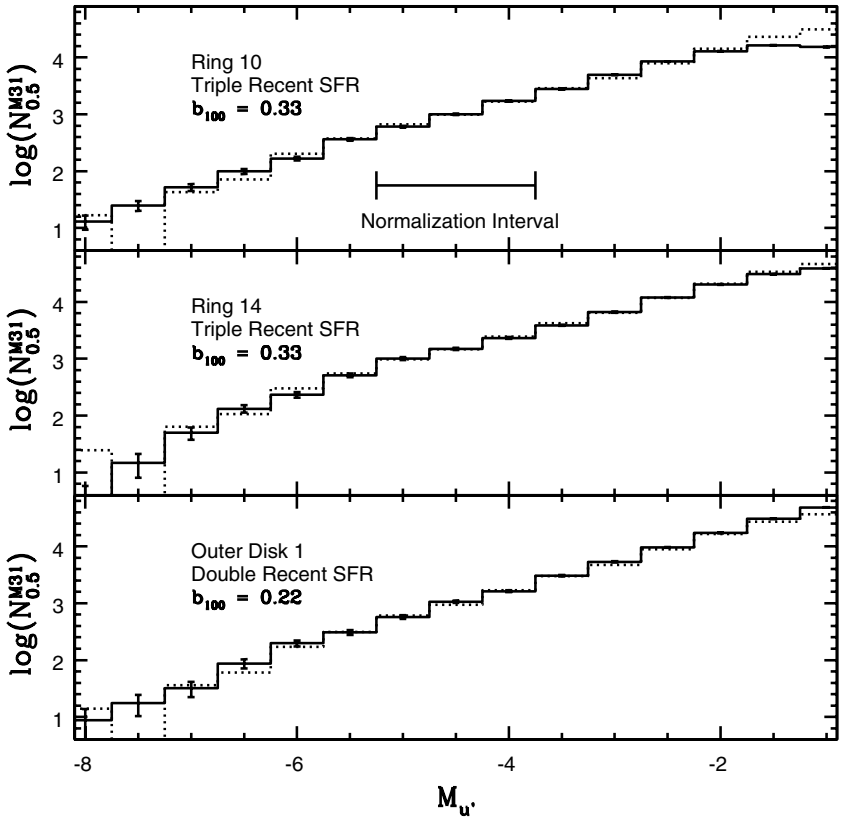

Figure 15. Same as Figure 13, but showing models that assume a cSFR for $t > 10$ Myr and an increase in the SFR when $t < 10$ Myr. b_{100} is the ratio of the number of stars that formed within the past 10 Myr to those that formed 10–100 Myr in the past; $b_{100} = 0.11$ for a cSFR. The Outer Disk 2 LF is not shown, as it is adequately represented by the cSFR model (Figure 14). Models with elevated recent SFRs provide a better match to the LFs shown here than the cSFR models.

6. THE SPATIAL DISTRIBUTION OF STARS IN THE M31 DISK

6.1. Young Main-sequence Stars

The spatial distribution of stars in a known age range is an important probe of galaxy evolution. Samples of YMS stars (ages <10 Myr) and intermediate-age main-sequence stars (IMS; ages ∼100 Myr) were selected from the MegaCam data based on their location in the $(g', u' - g')$ CMD. The boundaries of the YMS and IMS regions in Figure 16 were defined using isochrones as guides, while also keeping in mind the results of the artificial star and stacking experiments discussed in Section 3.

The distributions of objects in the YMS and IMS samples are shown in Figures 17 (as observed on-sky) and 18 (as would be observed face-on). The face-on distributions assume that the stars are in an infinitely thin, unwarped disk, and departures from these assumptions will cause blurring of structures in the de-projected distributions. Some blurring is expected, as the gas disk of M31 is warped (Corbelli et al. 2010).

It is evident from Figures 17 and 18 that (1) recent star-forming activity in M31 has not been uniformly distributed with azimuthal angle and (2) knots of stars in both samples are seen throughout the disk. The stars in the YMS sample tend to be tightly clustered and define partial arcs. The distribution of YMS stars indicates that the most intense area of recent star formation was in the northeast quadrant of the disk.

There is broad agreement between the YMS distribution and images of UV (Figure 1 of Thilker et al. 2005) and MIR (Figure 1 of Gordon et al. 2006) emission. While peaks in H I emission shown in Figure 1 of Unwin (1983) coincide with areas of high YMS density in Ring 10, at radii <47 arcmin ($R_{GC} < 10$ kpc) there are collections of YMS stars with no corresponding H I feature. In contrast, there is much better agreement between the location of YMS concentrations and the peaks in CO (1–0) emission mapped by Nieten et al. (2006).

Stars in the YMS sample are seen at moderately small R_{GC}. Large-scale, well-defined structures that contain bright blue stars are seen near 20 arcmin (i.e., $R_{GC} = 4$ kpc), while individual objects in the YMS sample are detected to within 10 arcmin ($R_{GC} \sim 2$ kpc) of the nucleus. This R_{GC} is where the bulge and disk contribute comparable amounts of light at visible wavelengths (e.g., Tempel et al. 2011) and where the FUV–NUV color in the main body of the galaxy is reddest (Thilker et al. 2005).

Ring structures are much more pronounced in the IMS distribution than in the YMS distribution. The IMS sample contains stars that formed over a wider range of ages than the YMS stars, and so the effects of spatial fluctuations in star-forming activity are expected to average out. The more or less uniform azimuthal distribution of IMS objects in the rings suggests that the location of star formation in the immediate past differed from the present day, and that areas of active star formation in the rings have moved through a wide range of position angles within M31.

That Ring 10 is seen in samples of objects that are as old as 100 Myr indicates that the event that spurred its formation must have occurred at least 100 Myr ago. In fact, it is somewhat surprising that rings and arcs are present at all in the IMS sample, given the rate at which stars in the disks of nearby star-forming galaxies acquire random velocities with time as they interact with GMCs. The velocities acquired in this manner

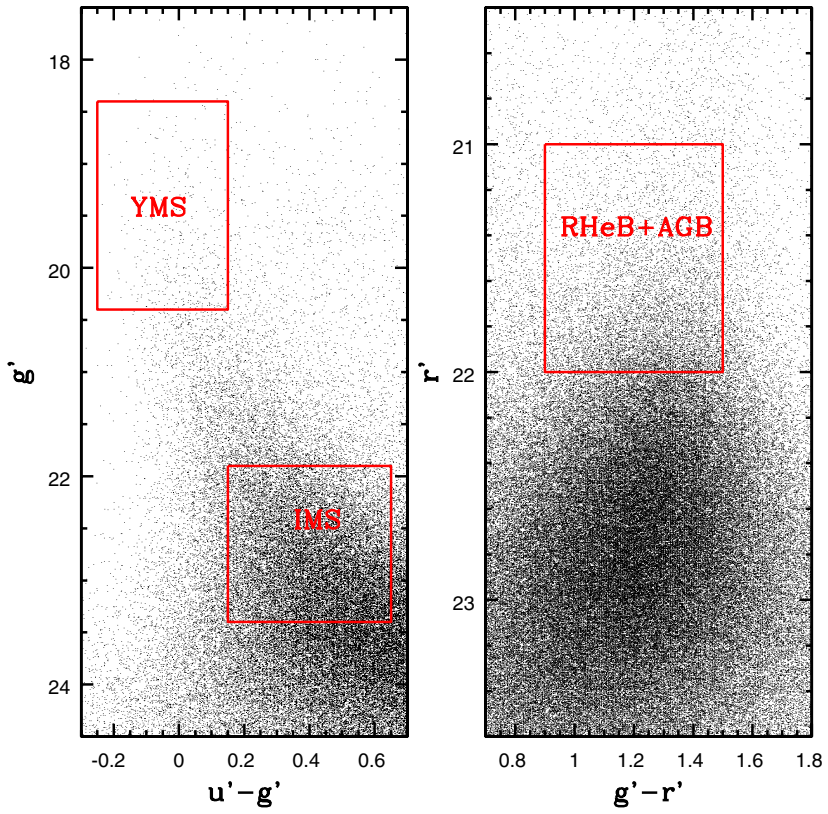

Figure 16. Sections of the $(g', u' - g')$ and $(r', g' - r')$ CMDs of Ring 10. The areas that are used to identify the samples of young main-sequence (YMS), intermediate-age main-sequence (IMS), and RHeB+AGB objects that are examined in Figures 17–20 are indicated.

(A color version of this figure is available in the online journal.)

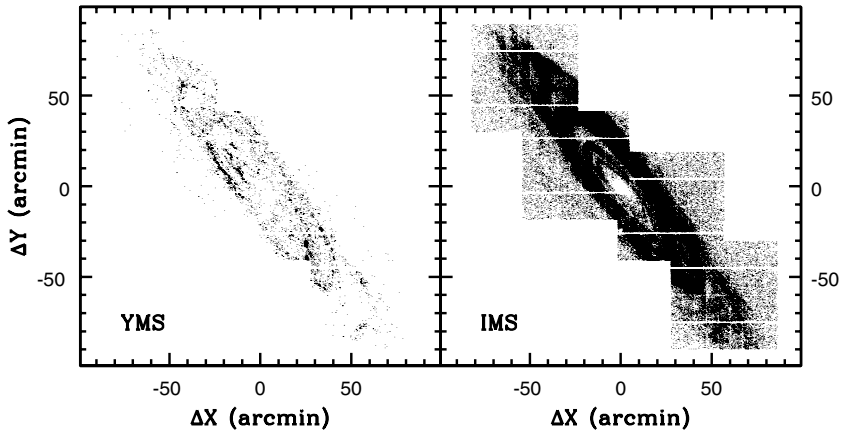

Figure 17. Distributions of sources in the YMS ($t \geqslant 10$ Myr) and IMS ($t \sim 100$ Myr) samples as observed on the sky. The x- and y-axes show distances in arcminutes from the center of the galaxy. Stars in the YMS sample are located throughout the disk, although they tend to congregate in rings and arcs. Rings are also evident in the IMS sample, indicating that these structures have ages $\geqslant$100 Myr.

can cause disk stars to move substantial distances over time spans of 100 Myr. For example, spiral structure in M33 is well defined by stars with ages $\leqslant$10 Myr but is not apparent in the distribution of stars with ages of 100 Myr (Davidge & Puzia 2011). The presence of organized structures in the disk of M31 that are defined by objects in the IMS sample suggests that stars in these parts of M31 do not attain the same random motions as their counterparts in M33. The narrow distribution of orbital angular momentum that is expected for star-forming material in rings undoubtedly contributes to restricting the time evolution of random velocities among stars in these structures.

6.2. Evolved Red Stars and Age Gradients

A sample of RHeB+AGB stars has been selected using the boundaries indicated on the $(r', g' - r')$ CMD in Figure 16. The objects in this part of the CMD formed 60–200 Myr in the past, and so probe earlier epochs than the IMS sample. The faint limit of the extraction region in Figure 16 reflects the results of the data characterization experiments discussed in Section 3.

The face-on distribution of objects in the RHeB+AGB sample is shown in Figure 19. The distribution observed on the sky is not shown, as the density of red sources makes it difficult to detect structure because of the orientation of M31 on the

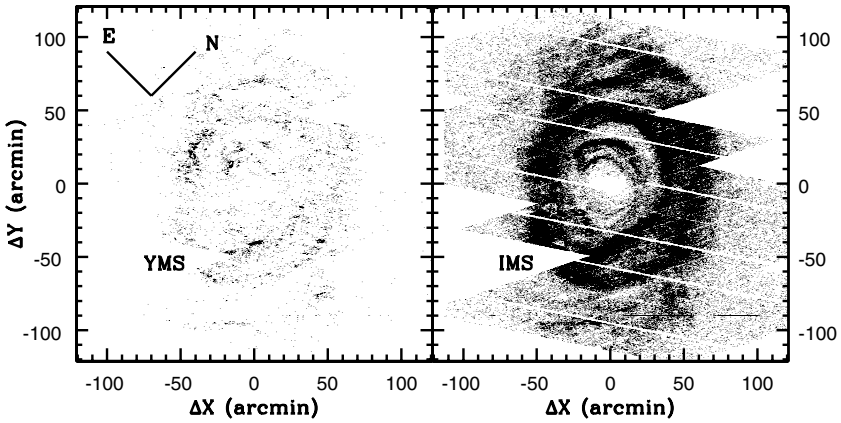

Figure 18. Same as Figure 17, but showing the distribution of objects as they would appear if M31 were viewed face-on. The orientation of M31 has been rotated so that the semimajor axis is vertical. North and east are indicated.

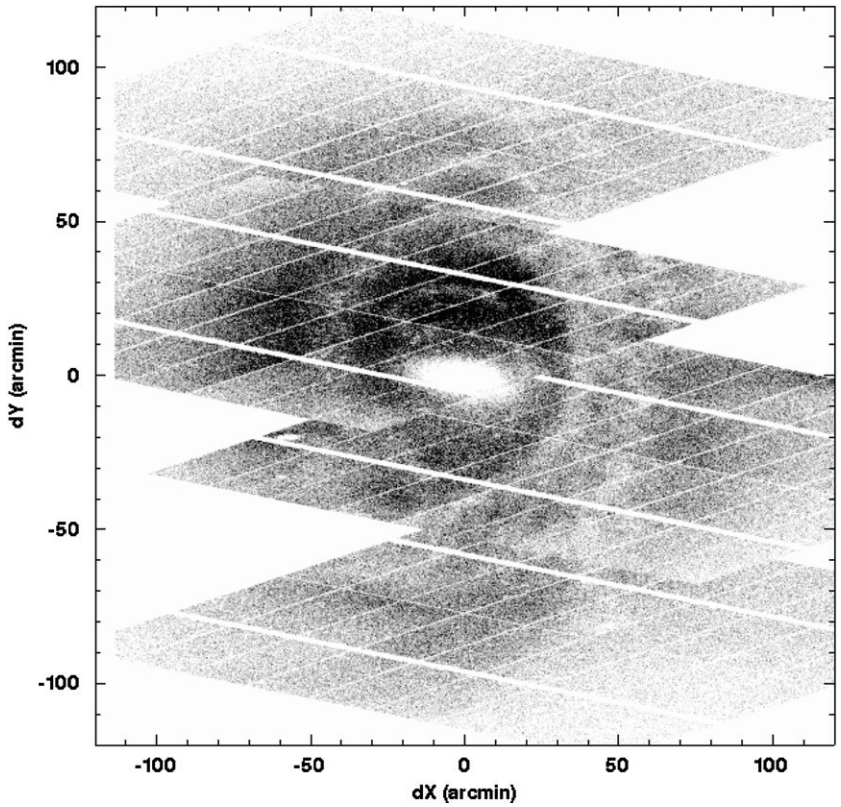

Figure 19. Distribution of sources in the RHeB+AGB sample, as they would appear if M31 were viewed face-on. The major axis of M31 points upward. The intensity at each location reflects number counts in 6 × 6 arcsec bins. The source distribution is asymmetric in the sense that the density of objects above the galaxy center is much higher than to the south of the galaxy center. M32 is located near $(dX, dY) = (-60, -20)$, while the concentration of sources near $(dX, dY) = (100, 0)$ is probably associated with NGC 205.

sky. As in Figure 18, the major axis of M31 points upward. The concentration near $(dX, dY) = (-60, -20)$ is centered on M32; the dense central regions of M32—where stars are not resolved—appears as a hole in the RHeB+AGB distribution. The concentration near $(dX, dY) = (100, 0)$ is probably associated with NGC 205 (see Figure 1).

The distribution of RHeB+AGB stars in Figure 19 is asymmetric about the horizontal axis, in the sense that the stellar density above and to the left of the galaxy center (i.e., along the northeast arm of the semimajor axis) is higher than that below the galaxy center. There are also asymmetries to the left and right of the galaxy center, which fall along the minor axis. However, the orientation of M31 on the sky is such that the distribution of objects along the minor axis is more prone to uncertainties arising from—for example—the inherent thickness of the disk and the presence of stars in the bulge of M31, both of which may affect the de-projected stellar distribution. We thus focus on the asymmetry along the major axis, where the de-projected distribution is most secure.

Number counts in an 8 arcmin wide strip along the northeast and southwest segments of the major axis are shown in Figure 20. The density of RHeB+AGB stars along the NE axis within 50 arcmin (∼10 kpc) of the galaxy center is higher than along the SW axis. At $\Delta Y = 25$ arcmin these stars have a density that is 0.4 dex higher on the NE axis than at the same point on the SW axis. This suggests that the northeast part of the galaxy

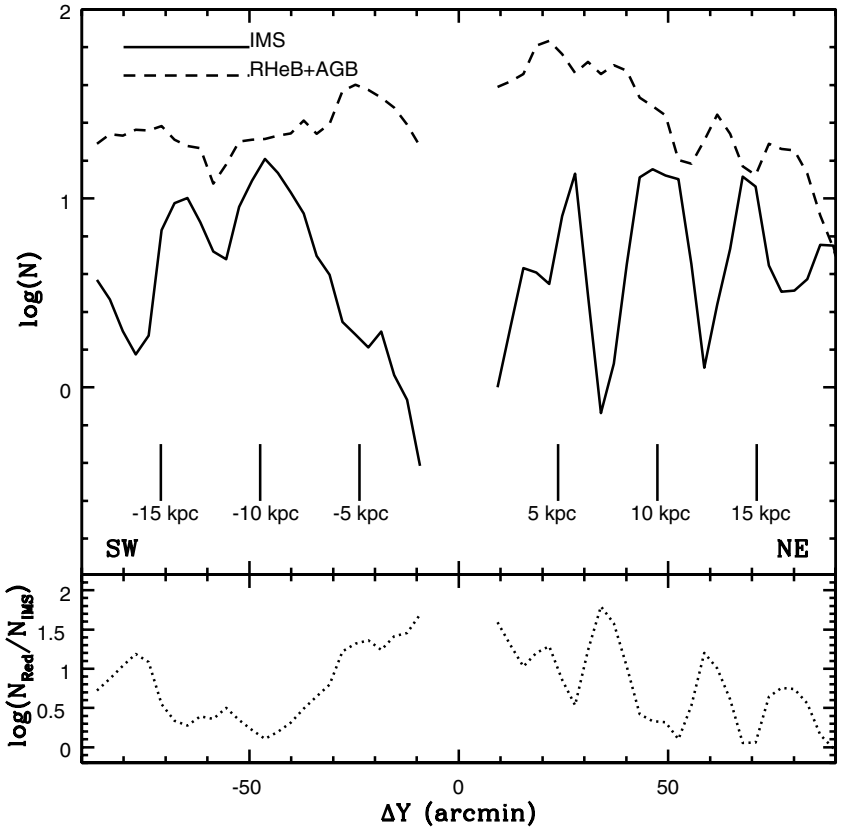

Figure 20. Top panel: the distribution of RHeB+AGB and IMS objects along the major axis of M31. N is the number of stars arcmin^{-2} in the de-projected data set within ±4 arcmin of the major axis. Positive distances are along the NE axis, while negative distances are along the SW axis. The number density of evolved red stars is ∼0.4 dex higher at $R = 5$ kpc than at $R = -5$ kpc; the distribution of these objects in M31 is thus lopsided. The spatially periodic nature of recent star-forming regions is also clearly evident in the IMS profile along the NE axis. Bottom panel: the ratio of stars in the RHeB+AGB and IMS samples. The peaks due to star-forming rings aside, there is a tendency for the ratio to decrease toward larger radii along the NE axis, indicating that the relative frequency of younger stars grows with increasing radius.

was an area of more intense star-forming activity 100+ Myr in the past than the southwest part. Persistent large-scale concentrations of elevated star-forming activity are seen in other nearby disk galaxies, such as NGC 253 (Davidge 2010).

The number counts of objects in the IMS sample are also shown in Figure 20, and it is evident that the IMS and RHeB+AGB samples have very different radial distributions. Star-forming rings form a 5 kpc periodicity in the distribution of IMS stars, and these structures are most pronounced along the NE axis. The rings have an amplitude of ∼1 dex in the IMS counts. The red stars show more gradual variations with radius, and there is little or no correlation with features in the IMS distribution. Departures from large-scale trends in the RHeB+AGB distribution are substantially smaller than those in the IMS distribution, amounting to ∼0.2 dex.

In addition to the periodic nature of structure in the radial distribution of IMS stars, there is also a systematic gradient in the relative numbers of RHeB+AGB and IMS stars. This is investigated in the lower panel of Figure 20, where the ratio of objects in the two samples is shown. There is a tendency for the numbers of RHeB+AGB and IMS sources to become more equal toward larger R_{GC}, indicating that star formation was more centrally concentrated in M31 during intermediate epochs than at present. This trend is most noticeable when considering sources along the NE axis; while a gradient is seen out to $R_{GC} \sim 10$ kpc along the SW axis, it may reverse at larger radii. We note that the FUV–NUV color in M31 decreases (i.e., becomes bluer) toward larger radii in the Inner Disk when $R_{GC} > 2$ kpc (Thilker et al. 2005), and this is broadly consistent with the relative radial distributions of the RHeB+AGB and IMS objects in our data. The change in UV color in the interval $R_{GC} \leqslant 10$ kpc corresponds to a change in luminosity-weighted SSP age from >450 Myr to 290 Myr (Thilker et al. 2005).

Ferguson et al. (2002) investigate the distribution of RGB and AGB stars in the outer regions of the M31 disk. Their study intentionally avoids the main body of the disk where crowding is an issue for their aperture photometry measurements, and so there is only modest spatial overlap between our MegaCam and the Ferguson et al. (2002) data sets. Still, we note that Figure 2 of Ferguson et al. (2002) shows filamentary structure at large radii. While contamination from background galaxies accounts for a progressively larger fraction of the objects in Figure 19 as one moves to larger R_{GC}, there are hints of structures at large R_{GC} in Figure 19. These will prove to be promising targets for future deep photometric studies.

7. DISCUSSION AND SUMMARY

Images obtained with the CFHT MegaCam of the Local Group galaxy M31 have been used to examine the spatial distribution and photometric properties of the brightest stars in this system. M31 is an important target for studies of galaxy evolution not only because it is the closest external large disk galaxy, but also because it has anemic star-forming activity at the present day and is the nearest example of a red disk that is evolving in the so-called green valley. With four MegaCam

pointings we cover most of the M31 disk out to 100 arcmin ($R_{GC} \sim 20$ kpc) along the major axis, allowing us to investigate large-scale trends in stellar content. The primary goals of our study are (1) to probe the SFH of M31 during the past few hundred Myr and (2) to search for evidence of recent interactions.

When considered alongside studies of the outer regions and bulge of M31, which have yielded insights into the evolution of the galaxy during early and intermediate epochs, the results of the current work help to develop an understanding of the evolution of M31 in the context of other nearby galaxies. M31 has been subjected to interactions with companions (e.g., Section 1), and this activity has likely continued to cosmologically recent epochs. These interactions have influenced the large-scale redistribution of stars and gas and have had a major influence on the SFH of the galaxy. In the remainder of this section we discuss our four principal results: (1) the nature of the SFH during the past 100 Myr, focusing on the apparent rise in the SFR over the last ∼10 Myr that has occurred throughout much of the galaxy; (2) the spatial distribution of stars that formed 10–100 Myr in the past; (3) the distribution of evolved red stars that formed 100+ Myr ago; and (4) the subdued level of star-forming activity at the present day and the evolutionary status of M31.

7.1. The Recent SFH: Evidence for a Rise in the SFR

Stellar density changes with location in M31, and this affects the spatial coverage of the stellar samples used to probe the SFH. Because they are among the brightest stars in the galaxy and have relatively blue colors when compared with the underlying disk, main-sequence stars with ages ∼10 Myr are detected over a large fraction of the M31 disk. While resolving fainter stars is more challenging, main-sequence stars with ages ∼100 Myr are still detected at $R_{GC} \geqslant$ a few kpc in our data. The recent (i.e., within a hundred Myr) SFH can thus be investigated over much of the M31 disk.

The u' LFs of main-sequence stars are indicative of a cSFR during the past 10–100 Myr and so suggest that any major disturbance to the disk of M31 during intermediate epochs probably occurred more than ∼100–200 Myr in the past. However, the number counts of the brightest main-sequence stars indicate that the SFR has increased by a factor of 2–3 during the past ∼10 Myr. That this upturn in the SFR was not restricted to Ring 10 and Ring 14, which are the areas of M31 that contain a large fraction of its young stars and star-forming material, indicates that the trigger was an event that spurred activity throughout the disk and is probably not stochastic in nature.

A rise in star-forming activity during the past 10 Myr is not seen at $R_{GC} > 21$ kpc, and this provides clues into the nature of any event that may have triggered the change in the SFR. If the SFR was elevated by an interaction with a companion, then the point of closest encounter between M31 and this companion would have been $R_{GC} < 21$ kpc (e.g., Hopkins et al. 2009). If the companion passed through the disk plane, then the point of impact must have been in the present-day star-forming disk. Gordon et al. (2006) model an interaction with M32, in which that galaxy passed through the inner disk of M31 roughly 20 Myr ago. The timing of that event does not differ greatly from our estimate of a recent upswing in the disk SFR.

Large-scale spiral structure is often associated with recent interactions. If M32 (or another companion) passed through the disk of M31 in the recent past, then why is there no large-scale spiral structure? The amplitude of any spiral pattern depends on the mass of the perturber and the cold gas content of the larger galaxy. In addition, interactions may spur spiral structure only over limited areas, and even then these will survive only over dynamical timescales (Revaz et al. 2009). If M31 was depleted of cold gas—or the cold gas distribution was disrupted—prior to the most recent interaction with a companion, then prominent spiral structure may not be expected.

The SFH measured from the MegaCam images is broadly consistent with that presented by Williams (2002, 2003). Williams (2002) examined a suite of *HST*/WFPC2 images to investigate the SFHs of the M31 disk and its environs. Given the widely distributed locations of these fields, coupled with *HST*/WFPC2's modest science field, it is perhaps not surprising that there is a substantial field-to-field dispersion in the SFHs found from these data. Still, the SFHs for the majority of his fields are consistent with a cSFR during the past few hundred Myr, in agreement with the SFH deduced from the MegaCam u' LFs of main-sequence stars during the time interval 10–100 Myr.

Not all of the *HST*/WFPC2 fields show evidence of an upturn in the SFR within the past 10–20 Myr. This is perhaps not surprising, as the distribution of young stars, UV light, MIR emission, and molecular material all indicate that the recent rise in star-forming activity occurred in isolated areas that are distributed throughout the disk. The SFHs deduced from the MegaCam data are based on stellar content that covers substantial swaths of the M31 disk. The sampling of small star-forming areas by the substantially smaller *HST*/WFPC2 field will be less complete.

Williams (2003) used wide-field ground-based images that cover a total area of 1.4 deg^2 to probe the recent SFH of the M31 disk. The level of star-forming activity was found to decline by 50% from ∼250 Myr to ∼50 Myr in the past, although the SFR during the past 64 Myr is steady to within $\pm 0.1\ M_{\odot}\ \mathrm{yr}^{-1}$, thereby approximating a cSFR to within ± 20%. The SFR was also found to increase during the past 25 Myr, in broad agreement with the results found here. The qualitative agreement with the Williams (2003) results is significant, as Williams examined a much smaller portion of the disk and used a CMD-fitting technique that relies on stars spanning a range of evolutionary states, in contrast to our study, which is based on main-sequence stars.

7.2. Signatures of Recent Interactions: Characterizing Coherent Structures in the Disk of M31

Many bright main-sequence stars in M31 are found in ring- and shell-like structures. These rings have a radial periodicity of ∼5 kpc and—based on main-sequence stars that formed within the past 100 Myr—a stellar density that is an order of magnitude higher than in the inter-ring regions (Figure 20). Such a distribution of young stars indicates that much of the cool gas in M31 has been displaced systematically throughout M31, as is evident in the distribution of H I and molecular material (e.g., Emerson 1974; Nieten et al. 2006).

The distribution of objects in the IMS sample indicates that the rings have been in place (and forming stars) for at least ∼100 Myr. GMCs in the disks of "normal" star-forming galaxies play a key role in kinematically heating stars over time spans of a few tens of Myr. The modest physical width of the rings in M31 (±1 kpc; Figure 20) suggests that the orbital angular momenta of GMCs in these rings must have a compact distribution, reducing

the incidence of collisions and thus contributing to the longevity of these structures.

The IMS sample contains main-sequence stars that formed over the entirety of the past ∼100 Myr, and this might skew age estimates. Still, the majority of objects in the IMS sample likely have ages that are not much younger than 100 Myr. Indeed, there has been ongoing star formation throughout the disk of M31 during the past 100 Myr (Section 5), which proceeded at a pace that is consistent with a cSFR for $t > 10$ Myr. Given this SFH and the relation between age and MSTO magnitude, the majority of objects in the IMS sample will likely have ages that are weighted toward the older, as opposed to younger, end of the age range covered by the part of the ($M_{g'}$, $u' - g'$) CMD that contains IMS stars.

Interactions can produce the ring-like distribution of young stars in the M31 disk. Hammer et al. (2010) find that a gas ring forms in models in which M31 merges with a large companion on a polar orbit. Block et al. (2006) discuss a model in which a companion passed through the central regions of M31 ∼200 Myr ago. A propagating density wave, similar to that in the Cartwheel galaxy, then triggers star formation as it works its way outward. Block et al. (2006) suggest that the companion that spurred this event was M32, accompanied by a massive halo to enhance the strength of the interaction. However, the orbit that they assign to M32, together with its velocity, places it behind M31, whereas there is strong evidence that M32 lies in front (Ford et al. 1978). In any event, the spatial pattern of the IMS sample argues against this model. Rather than commencing at its current location only within the last 10 Myr or so, we find that the star formation in Ring 10 has existed for at least 100 Myr. The existence of similar long-lived star-forming structures outside Ring 10, such as Ring 14, is further evidence against a propagating wave origin for Ring 10.

In order to have a cSFR during the past ∼100 Myr, it is likely that the last major interaction between M31 and a companion occurred at least ∼500 Myr in the past. This leads us to speculate that the displacement of cool gas into rings may be an artifact of the event that triggered the last major upswing in star-forming activity 1–2 Gyr ago. The event that produced this rise in star-forming activity undoubtedly affected the ISM of M31 given the large population of globular clusters that formed at this time (Puzia et al. 2005).

Hammer et al. (2010) argue that the 10 kpc ring may have resulted from a merger between M31 and a large companion more than 5 Gyr ago. There are other possible perturbers: M33 is one, while another is M32 (or its progenitor). M32 is of interest as it contains a substantial population of stars with an age of a few billion years (e.g., Davidge 1990b, 2000; del Burgo et al. 2001; Worthey 2004; Rose et al. 2005) that are uniformly distributed throughout the galaxy (Davidge & Jensen 2007). The properties of M32 are also consistent with it having been sculpted by interactions. Compact elliptical galaxies like M32 are associated with dense environments, and there is evidence that the morphology of M32 may have changed dramatically with time. Indeed, remnants of a fossil disk have been detected around M32 (Graham 2002; Choi et al. 2002), suggesting that the present-day galaxy started out as a much larger disk system. M32 also lacks an entourage of globular clusters, as well as interstellar gas (Sage et al. 1998) and dust (Gordon et al. 2006). These components may have been removed if M32 was subjected to tidal stripping. The total mass of M32 is only ∼2% that of M31, and it is not clear that it would be large enough to influence star formation in M31, although if it interacted with M31, then its initial mass was probably larger than at the present day. Simulations suggest that satellites with masses that are 10% of the larger system can significantly affect disk properties (Mori & Rich 2008; Qu et al. 2011).

The events that re-distributed gas and spurred elevated levels of star formation may leave signatures near the disk boundary. Mergers are expected to move the boundaries of stellar disks outward (e.g., Younger et al. 2007; Cook et al. 2009), as gas that loses angular momentum and moves inward scatters stars to larger radii, pushing out the radial extent of the disk. In fact, an extended disk is observed in M31 (e.g., Ferguson & Johnson 2001) and is traced out to ∼40 kpc (Ibata et al. 2005). The outer regions of the disk account for 10% of the total M31 disk luminosity (Ibata et al. 2005), indicating that it is a significant structural component. Ferguson & Johnson (2001) also conclude that the majority of stars in the outer disk have ages in excess of a Gyr, which is consistent with a population of stars that were displaced outward during the event that produced the population of intermediate-age globular clusters. In contrast, Ibata et al. (2005) and Peñarrubia et al. (2006) argue that this part of the disk is the product of satellite accretion, rather than the re-configuring of the orbits of stars that originated at smaller radii.

7.3. Signatures of Recent Interactions: The Asymmetric Distribution of Evolved Red Stars

Lopsided structure in galaxies is not rare (e.g., Zaritsky & Rix 1997) and may be a signature of the large-scale radial movement of gas in disks (e.g., Reichard et al. 2009), or the non-uniform accretion of cosmic gas (Bournaud et al. 2005). The projected density of RHeB+AGB stars with $R_{GC} < 10$ kpc along the NE segment of the major axis is roughly two times that along the SW segment. Given that these stars have ages 100–200 Myr, the lopsided distribution was likely spurred by an event that occurred within the past ∼0.5 Gyr. Such a timescale would allow an elevated SFR to die down so that a cSFR could be seen in the time interval probed by the u' LF of main-sequence stars in the Inner Disk.

The asymmetric distribution of RHeB+AGB stars is consistent with other observations. Williams (2003) found that the region ∼20–30 arcmin of the northeast of the galaxy center was an area of enhanced star-forming activity 64–256 Myr in the past. In addition, circumstellar envelopes around massive AGB stars contribute significantly to the MIR light from systems containing stars that formed within the past few Gyr. The [5.8] and [8.0] major-axis profiles of M31 shown in Figure 2 of Barmby et al. (2006) have higher levels of emission between ∼800 and 1800 arcsec (13–30 arcmin) along the NE major-axis segment than the corresponding section of the SW segment. Davidge (2012) examined 2MASS images and discovered a substantial concentration of AGB stars ∼3.5 kpc NE of the center of M31. This structure is populated by stars with ages in excess of 100 Myr.

The presence of a large-scale asymmetry in the distribution of stars with ages 100–200 Myr is perhaps surprising given that rotational shear might be expected to blur such structures. However, shear will not be an issue for stars at radii where the disk kinematics follow solid-body rotation. While rotation curves derived from H I suggest that significant shear might be expected even in the inner regions of M31 (e.g., Braun 1991), the gas dynamics at small radii may not reflect those of objects in the stellar disk (e.g., Kent 1989a). Still, there is agreement between the rotational properties of M31 defined by H I and

planetary nebulae at $R_{GC} \sim 12$ kpc (Halliday et al. 2006), and the rotation velocity measured from H II regions drops near 25–30 armin ($R_{GC} \sim 5$–6 kpc; Kent 1989b). For comparison, the asymmetry in the RHeB+AGB number counts disappears when $R_{GC} > 10$ kpc. Kinematic measurements of bright AGB stars in the inner disk of M31 will help establish whether they are in the disk plane. Such measurements could be made in the K band, where the brightest AGB stars in M31 have $K \leqslant 17$ and significant gains in angular resolution can be realized with adaptive optics systems.

The event that produced the asymmetric distribution of RHeB+AGB stars may have left signatures in the extraplanar regions if it involved an encounter with a satellite. The GSS, which Mori & Rich (2008) model as the result of a moderate-mass companion passing through the M31 disk, is one candidate signature of such an event. Fardal et al. (2007) find a kinematic age for the GSS of 750 Myr, which is a few hundred Myr older than the RHeB+AGB stars examined here.

The dwarf elliptical galaxy NGC 205 is one of the largest companions of M31 and has a projected distance of only ∼10 kpc from the center of M31. Twisting of the outer isophotes of NGC 205 is consistent with tidal disruption (Choi et al. 2002). There is evidence in the resolved stellar content of NGC 205 for a large episode of star formation ∼100 Myr in the past and another a few hundred Myr before that (Davidge 2003). The timing of the first event coincides with the last M31 disk crossing predicted by Cepa & Beckman (1988), while the second is consistent with their period of NGC 205 about M31. The second star-forming episode is also consistent with the timing of the event that may have produced the lopsided distribution of RHeB+AGB stars in M31.

Howley et al. (2008) re-examine the orbital properties of NGC 205 and suggest that it might be on its first passage by M31, counter to the orbit proposed by Cepa & Beckman (1988). If NGC 205 has interacted with M31, then a tidal tail would be expected, and McConnachie et al. (2004) report the possible detection of such a structure. Given that there is no consensus or firm evidence on the orbit of NGC 205 about M31, the connection between this satellite and the larger galaxy must remain speculative for now.

7.4. M31 as a Red Disk Galaxy

Photometric surveys of galaxies reveal distinct red and blue sequences on CMDs (e.g., Strateva et al. 2001; Bell et al. 2004). The majority of objects in the blue sequence are disk dominated, while the majority of objects in the red sequence are spheroid dominated (Strateva et al. 2001). Mutch et al. (2011) examine the morphology and integrated colors of M31 and conclude that it is currently in the "green valley" that falls between the blue and red sequences. They also conclude that at least one in six nearby disk galaxies, including the Galaxy, lie in the green valley or on the red sequence. If the SFR of M31 has recently increased by a factor of 2–3, then the appearance of M31 ∼100 Myr in the past would have been different from the present day. If the current SFR is one-third that of M33, for which the SFR is 0.5–0.7 $M_{\odot}$ yr^{-1} (Hippelein et al. 2003; Verley et al. 2009), then the SFR in M31 would have been only 0.1 $M_{\odot}$ yr^{-1} a hundred Myr ago. When considered in the context of star-forming activity, M31 at that time would have appeared as a largely dead system.

The sSFR in M31 is similar to that in nearby red disk galaxies, such as the lenticular galaxy NGC 5102. Using the integrated K-band brightnesses of M31 and NGC 5102 from Jarrett et al. (2003) as proxies for computing relative stellar masses, and assuming an SFR of ∼0.02 $M_{\odot}$ yr^{-1} for NGC 5102 (Davidge 2008), the sSFR of M31 100 Myr ago would have been comparable to that of NGC 5102 at the present day. It is perhaps worth noting that M31 and NGC 5102 share common morphological properties. Young stars in NGC 5102 have a ring-like distribution, and the lopsided distribution of AGB stars in NGC 5102 (Figure 5 of Davidge 2010) is reminiscent of the distribution of RHeB+AGB stars in M31.

Bundy et al. (2010) examine the morphologies of red sequence galaxies and find that a significant number are passively evolving disks where large-scale star formation has ceased. The red disk galaxies examined by Bundy et al. (2010) tend to have more prominent bulges than blue, star-forming disk galaxies. Red disk galaxies are found in a range of environments, suggesting that they are not the exclusive product of evolution in high-density regions. The stellar archeology of M31 may provide clues into how red disk galaxies evolve in environments like the Local Group.

Star formation in galaxies is influenced by a number of factors, one of which is environment, and galaxies with companions tend to have high sSFRs (Li et al. 2008). The sSFR also depends on galaxy mass, in the sense that the sSFR at the present day rises as one moves to lower masses (e.g., Kauffmann et al. 2003). Bundy et al. (2010) suggest that star formation in red disks may have been halted by mergers and subsequent interactions. These events would have driven the rapid consumption of star-forming material and ultimately contributed to the disruption of the cold ISM. Red sequence disks are expected to evolve into pressure-supported systems if they experience a major merger, as there is no cool gas from which a disk could re-form.

To the extent that M31 can be considered to be a typical red disk galaxy, its past history appears to favor the "two stage" model forwarded by Bundy et al. (2010), in which a disk is first stripped of gas and is then pummeled by other systems to produce a red galaxy that is supported mainly by random motions, rather than rotation. The final pressure-supported configuration of M31 may be realized a few Gyr in the future, when it is projected to merge with the Galaxy (e.g., Cox & Abraham 2008). Barring an injection of cool gas into the M31 disk during the next few Gyr, this merger will occur when M31 is gas-poor and—based on the present-day modest SFR—contains a preponderance of stars with ages in excess of a few Gyr.

G.F.L. thanks the Australian Research Council for support through his Future Fellowship (FT100100268) and Discovery project (DP110100678). Financial support for this work was provided in part by the POMMME project (ANR 09-BLAN-0228). We thank the anonymous referee for comments that improved the manuscript.

Note added in proof. While this paper was being readied for publication, we became aware of the study of Azimlu et al. (2011), who find evidence for an increase in the star-forming activity of M31 15–20 Myr ago based on the properties of H II regions.

REFERENCES

Azimlu, M., Marciniak, R., & Barmby, P. 2011, AJ, 142, 139
Barmby, P., Ashby, M. L. N., Bianchi, L., et al. 2006, ApJ, 650, L45
Bastian, N. 2008, MNRAS, 390, 759
Beasley, M. A., Brodie, J. P., Strader, J., et al. 2004, AJ, 128, 1623
Beasley, M. A., Brodie, J. P., Strader, J., et al. 2005, AJ, 129, 1412

Beaton, R. L., Majewski, S. R., Guhathakurta, P., et al. 2007, ApJ, 658, L91
Bekki, K. 2008, MNRAS, 390, L24
Bekki, K., & Chiba, M. 2001, ApJ, 558, 666
Bell, E. F., Wolf, C., Meisenheimer, K., et al. 2004, ApJ, 608, 752
Bender, R., Kormendy, J., Bower, G., et al. 2005, ApJ, 631, 280
Bica, E., Barbuy, B., & Ortolani, S. 1991, ApJ, 382, L15
Bigiel, F., Leroy, A., Walter, F., et al. 2010, AJ, 140, 1194
Block, D. L., Bournaud, F., Combes, F., et al. 2006, Nature, 443, 832
Boissier, S., & Prantzos, N. 1999, MNRAS, 307, 857
Bonanos, A. Z., Stanek, K. Z., Kudritzki, R. P., et al. 2006, ApJ, 652, 313
Boulade, O., Charlot, X., Abbon, P., et al. 2003, Proc. SPIE, 4841, 72
Bournaud, F., Combes, F., Jog, C. J., & Puerari, I. 2005, A&A, 438, 507
Braun, R. 1991, ApJ, 372, 54
Braun, R., & Thilker, D. A. 2004, A&A, 417, 421
Brown, T. M., Beaton, R., Chiba, M., et al. 2008, ApJ, 685, L121
Bruzual, G., & Charlot, S. 2003, MNRAS, 344, 1000
Bundy, K., Scarlata, C., Carollo, C. M., et al. 2010, ApJ, 719, 1969
Burstein, D., Faber, S. M., Gaskell, C. M., & Krumm, N. 1984, ApJ, 287, 586
Burstein, D., Li, Y., Freeman, K. C., et al. 2004, ApJ, 614, 158
Caldwell, N., Harding, P., Morrison, H., et al. 2009, AJ, 137, 94
Carretta, E., Bragaglia, A., Gratton, R. G., et al. 2010, A&A, 516, 55
Cepa, J., & Beckman, J. E. 1988, A&A, 200, 21
Chapman, S. C., Ibata, R., Lewis, G. F., et al. 2006, ApJ, 653, 255
Choi, P. I., Guhathakurta, P., & Johnston, K. V. 2002, AJ, 124, 310
Cole, A. A., & Weinberg, M. D. 2002, ApJ, 574, L43
Collins, M. L. M., Chapman, S. C., Ibata, R. A., et al. 2011, MNRAS, 413, 1548
Cook, M., Lapi, A., & Granato, G. L. 2009, MNRAS, 397, 534
Cooper, A. P., Cole, S., Frenk, C. S., et al. 2010, MNRAS, 406, 744
Corbelli, E., Lorenzoni, S., Walterbos, R., Braun, R., & Thilker, D. 2010, A&A, 511, 89
Cox, T. J., & Abraham, L. 2008, MNRAS, 386, 461
Daddi, E., Elbaz, D., Walter, F., et al. 2010, ApJ, 714, L118
Dalcanton, J. J., & PHAT Collaboration 2011, BAAS, 43, 2011
Davidge, T. J. 1990a, ApJ, 351, L37
Davidge, T. J. 1990b, AJ, 99, 561
Davidge, T. J. 1997, AJ, 113, 985
Davidge, T. J. 2000, PASP, 112, 1177
Davidge, T. J. 2001a, AJ, 121, 3100
Davidge, T. J. 2001b, AJ, 122, 1386
Davidge, T. J. 2003, ApJ, 597, 289
Davidge, T. J. 2008, AJ, 135, 1636
Davidge, T. J. 2010, ApJ, 725, 1342
Davidge, T. J. 2012, ApJ, 749, L7
Davidge, T. J., Alloin, D., & Jablonka, P. 1991, ApJ, 358, L1
Davidge, T. J., & Jensen, J. B. 2007, AJ, 133, 576
Davidge, T. J., Jensen, J. B., & Olsen, K. A. G. 2006, AJ, 132, 521
Davidge, T. J., & Puzia, T. H. 2011, ApJ, 738, 144
del Burgo, C., Peletier, R. F., Vazdekis, A., Arribas, S., & Mediavilla, E. 2001, MNRAS, 321, 277
de Vaucouleurs, G. 1978, ApJ, 223, 351
Devereux, N. A., Price, R., Wells, L. A., & Duric, N. 1994, AJ, 108, 1667
Durrell, P. R., Harris, W. E., & Pritchet, C. J. 2001, AJ, 121, 2557
Edvardsson, B., Andersen, J., Gustafsson, B., et al. 1993, A&A, 275, 101
Efremov, Y. N. 2010, MNRAS, 405, 1531
Emerson, D. T. 1974, MNRAS, 169, 607
Fardal, M. A., Babul, A., Guhathakurta, P., Gilbert, K. M., & Dodge, C. 2008, ApJ, 682, L33
Fardal, M. A., Guhathakurta, P., Babul, A., & McConnachie, A. W. 2007, MNRAS, 380, 15
Ferguson, A. M. N., Irwin, M. J., Ibata, R. A., Lewis, G. F., & Tanvir, N. R. 2002, AJ, 124, 1452
Ferguson, A. M. N., & Johnson, R. A. 2001, ApJ, 559, L13
Firmani, C., & Avila-Reese, V. 2009, MNRAS, 396, 1675
Font, A. S., Johnston, K. V., Ferguson, A. M. N., et al. 2008, ApJ, 673, 215
Font, A. S., Johnston, K. V., Guhathakurta, P., Majewski, S. R., & Rich, R. M. 2006, AJ, 131, 1436
Forbes, D. A., & Bridges, T. 2010, MNRAS, 404, 1203
Ford, H. C., Jacoby, G. H., & Jenner, D. C. 1978, ApJ, 223, 94
Fuentes-Carrera, I., Jablonka, P., Sarajedini, A., et al. 2008, A&A, 483, 769
Fukugita, M., Ichikawa, T., Gunn, J. E., et al. 1996, AJ, 111, 1748
Fusi Pecci, F., Bellazzini, M., Buzzoni, A., et al. 2005, AJ, 130, 554
Gilbert, K. M., Fardal, M., Kalirai, J. S., et al. 2007, ApJ, 668, 245
Gilbert, K. M., Font, A. S., Johnston, K. V., & Guhathakurta, P. 2009, ApJ, 701, 776
Girardi, L., Grebel, E. K., Odenkirchen, M., & Chiosi, C. 2004, A&A, 422, 205
Gogarten, S. M., Dalcanton, J. J., Williams, B. F., et al. 2010, ApJ, 712, 858
Gordon, K. D., Bailin, J., Engelbracht, C. W., et al. 2006, ApJ, 638, L87
Governato, F., Willman, B., Mayer, L., et al. 2007, MNRAS, 374, 1479
Graham, A. W. 2002, ApJ, 568, L13
Grcevich, J., & Putman, M. E. 2009, ApJ, 696, 385
Halliday, C., Carter, D., Bridges, T. J., et al. 2006, MNRAS, 369, 97
Hammer, F., Flores, H., Puech, M., et al. 2009, A&A, 507, 1313
Hammer, F., Puech, M., Chemin, L., Flores, H., & Lehnert, M. 2007, ApJ, 662, 322
Hammer, F., Yang, Y. B., Wang, J. L., et al. 2010, ApJ, 725, 542
Harbeck, D., Grebel, E. K., Holtzman, J., et al. 2001, AJ, 122, 3092
Harris, J., & Zaritsky, D. 2001, ApJS, 136, 25
Hernandez, X., Valls-Gabaud, D., & Gilmore, G. 2000, MNRAS, 316, 605
Hippelein, H., Haas, M., Tuffs, R. J., et al. 2003, A&A, 407, 137
Hodge, P., Krienke, O. K., Bianchi, L., Massey, P., & Olsen, K. 2010, PASP, 122, 745
Hopkins, P. F., Cox, T. J., Younger, J. D., & Hernquist, L. 2009, ApJ, 691, 1168
Howley, K. M., Geha, M., Guhathakurta, P., et al. 2008, ApJ, 683, 722
Ibata, R., Chapman, S., Ferguson, A. M. N., et al. 2005, ApJ, 634, 287
Ibata, R., Irwin, M., Lewis, G., Ferguson, A. M. N., & Tanvir, N. 2001, Nature, 412, 49
Ibata, R., Martin, N. F., Irwin, M., et al. 2007, ApJ, 671, 1591
Jarrett, T. H., Chester, T., Cutri, R., Schneider, S. E., & Huchra, J. P. 2003, AJ, 125, 525
Kalirai, J. S., Gilbert, K. M., Guhathakurta, P., et al. 2006, ApJ, 648, 389
Kang, Y., Bianchi, L., & Rey, S.-C. 2009, ApJ, 703, 614
Kauffmann, G., Heckman, T. M., White, S. D. M., et al. 2003, MNRAS, 341, 54
Kennicutt, R. C., Jr., Lee, J. C., Funes, J. G., Sakai, S., & Akiyama, S. 2008, ApJS, 178, 247
Kent, S. M. 1989a, AJ, 97, 1614
Kent, S. M. 1989b, PASP, 101, 489
Koch, A., & Rich, R. M. 2010, AJ, 139, 2279
Koch, A., Rich, R. M., Reitzel, D. B., et al. 2008, ApJ, 689, 958
Kroupa, P., Tout, C. A., & Gilmore, G. 1993, MNRAS, 262, 545
Leitherer, C. 2001, in ASP Conf. Ser. 245, Astrophysical Ages and Time Scales, ed. T. von Hippel, C. Simpson, & N. Manset (San Francisco, CA: ASP), 390
Li, C., Kauffmann, G., Heckman, T. M., Jing, Y. P., & White, S. D. M. 2008, MNRAS, 385, 1903
Mackey, A. D., & Gilmore, G. 2004, MNRAS, 355, 504
Mackey, A. D., Huxor, A. P., Ferguson, A. M. N., et al. 2010, ApJ, 717, L11
Marcillac, D., Elbaz, D., Charlot, S., et al. 2006, A&A, 458, 369
Marcon-Uchida, M. M., Matteucci, F., & Costa, R. D. D. 2010, A&A, 520, 35
Martinez-Delgado, D., Gabany, R. J., Crawford, K., et al. 2010, AJ, 140, 962
Massey, P., Olsen, K. A. G., Hodge, P. W., et al. 2006, AJ, 131, 2478
Massey, P., Olsen, K. A. G., Hodge, P. W., et al. 2007, AJ, 133, 2393
Massey, P., Silva, D. R., Levesque, E. M., et al. 2009, ApJ, 703, 420
McConnachie, A. W., Ferguson, A. M. N., Irwin, M. J., et al. 2010, ApJ, 723, 1038
McConnachie, A. W., Irwin, M. J., Ibata, R., et al. 2003, MNRAS, 343, 1335
McConnachie, A. W., Irwin, M. J., Ibata, R. A., et al. 2009, Nature, 461, 66
McConnachie, A. W., Irwin, M. J., Lewis, G. F., et al. 2004, MNRAS, 351, L94
McQuinn, K. B. W., Skillman, E. D., Dalcanton, J. J., et al. 2011, ApJ, 740, 48
Melbourne, J., Williams, B., Dalcanton, J., et al. 2010, ApJ, 712, 469
Meylan, G., Sarajedini, A., Jablonka, P., et al. 2001, AJ, 122, 830
Montalto, M., Seitz, S., Riffeser, A., et al. 2009, A&A, 507, 283
Mori, M., & Rich, R. M. 2008, ApJ, 674, L77
Morrison, H., Caldwell, N., Schiavon, R. P., et al. 2011, ApJ, 726, L9
Mouhcine, M., & Lancon, A. 2003, A&A, 402, 425
Mould, J., & Kristian, J. 1986, ApJ, 305, 591
Munoz-Mateos, J. C., Gil de Paz, A., Boissier, S., et al. 2007, ApJ, 658, 1006
Mutch, S. J., Croton, D. J., & Poole, G. B. 2011, ApJ, 736, 84
Nieten, Ch., Neininger, N., Guélin, M., et al. 2006, A&A, 453, 459
Olsen, K. A. G., Blum, R. D., Stephens, A. W., et al. 2006, AJ, 132, 271
Oser, L., Ostriker, J. P., Naab, T., Johansson, P. H., & Burkert, A. 2010, ApJ, 725, 2312
Peñarrubia, J., McConnachie, A., & Babul, A. 2006, ApJ, 650, L33
Perina, S., Cohen, J. G., Barmby, P., et al. 2010, A&A, 511, 23
Pierce, M. J., & Tully, R. B. 1992, ApJ, 387, 47
Pritchet, C. J., & van den Bergh, S. 1988, ApJ, 331, 135
Putman, M. E., Peek, J. E. G., Muratov, A., et al. 2009, ApJ, 703, 1486
Puzia, T. H., Perrett, K. M., & Bridges, T. J. 2005, A&A, 434, 909
Qu, Y., Di Matteo, P., Lehnert, M. D., van Driel, W., & Jog, C. J. 2011, A&A, 535, A5
Reichard, T. A., Heckman, T. M., Rudnick, G., et al. 2009, ApJ, 691, 1005
Revaz, Y., Pfenniger, D., Combes, F., & Bournaud, F. 2009, A&A, 501, 171
Rice, W., Lonsdale, C. J., Soifer, B. T., et al. 1988, ApJS, 68, 91
Richardson, J. C., Ferguson, A. M. N., Mackey, A. D., et al. 2009, MNRAS, 396, 1842

Riess, A., Fliri, J., & Valls-Gabaud, D. 2012, ApJ, 745, 156
Robertson, B., Bullock, J. S., Cox, T. J., et al. 2006, ApJ, 645, 986
Robitaille, T. P., & Whitney, B. A. 2010, ApJ, 710, L11
Rose, J. A., Arimoto, N., Caldwell, N., et al. 2005, AJ, 129, 712
Roskar, R., Debattista, V. P., Stinson, G. S., et al. 2008, ApJ, 675, L65
Sage, L. J., Welch, G. A., & Mitchell, G. F. 1998, ApJ, 507, 726
Saglia, R. P., Fabricius, M., Bender, R., et al. 2010, A&A, 509, 61
Salpeter, E. E. 1955, ApJ, 121, 161
Sanchez-Blazquez, P., Courty, S., Gibson, B. K., & Brook, C. B. 2009, MNRAS, 398, 591
Schlegel, D. J., Finkbeiner, D. P., & Davis, M. 1998, ApJ, 500, 525
Sheth, K., Vogel, S. N., Wilson, C. D., & Dame, T. M. 2008, ApJ, 675, 330
Sil'chenko, O. K., Burenkov, A. N., & Vlasyuk, V. V. 1998, A&A, 337, 349
Smith, J. A., Tucker, D. L., Kent, S., et al. 2002, AJ, 123, 2121
Soto, K. T., & Martin, C. L. 2010, ApJ, 716, 332
Stetson, P. B. 1987, PASP, 99, 191
Stetson, P. B., & Harris, W. E. 1988, AJ, 96, 909
Stewart, K. R., Bullock, J. S., Wechsler, R. H., Maller, A. H., & Zentner, A. R. 2008, ApJ, 683, 597
Strateva, I., Ivezić, Ž., Knapp, G. R., et al. 2001, AJ, 122, 1861
Tabatabaei, F. S., & Berkhuijsen, E. M. 2010, A&A, 517, 77
Tanaka, M., Chiba, M., Komiyama, Y., et al. 2010, ApJ, 708, 1168
Tempel, E., Tuvikene, T., Tamm, A., & Tenjes, P. 2011, A&A, 526, A155
Teyssier, R., Chapon, D., & Bournaud, F. 2010, ApJ, 720, L149
Thilker, D. A., Hoopes, C. G., Bianchi, L., et al. 2005, ApJ, 619, L67
Trundle, C., Dufton, P. L., Lennon, D. J., Smartt, S. J., & Urbaneja, M. A. 2002, A&A, 395, 519
Unwin, S. C. 1983, MNRAS, 205, 773
van der Kruit, P. C., & Freeman, K. C. 2011, ARA&A, 49, 301
Verley, S., Corbelli, E., Giovanardi, C., & Hunt, L. K. 2009, A&A, 495, 453
Verley, S., Hunt, L. K., Corbelli, E., & Giovanardi, C. 2007, A&A, 476, 1161
Vilardell, F., Ribas, I., Jordi, C., Fitzpatrick, E. L., & Guinan, E. F. 2010, A&A, 509, 70
Walterbos, R. A. M., & Kennicutt, R. C., Jr. 1987, A&AS, 69, 311
Welch, G. A., Sage, L. J., & Mitchell, G. F. 1998, ApJ, 499, 209
Whitmore, B. C., Schweizer, F., Leitherer, C., Borne, K., & Robert, C. 1993, AJ, 106, 1354
Williams, B. E. 2002, MNRAS, 331, 293
Williams, B. E. 2003, AJ, 126, 1312
Worthey, G. 2004, AJ, 128, 2826
Yin, J., Hou, J. L., Prantzos, N., et al. 2009, A&A, 505, 497
Younger, J. D., Cox, T. J., Seth, A. C., & Hernquist, L. 2007, ApJ, 670, 269
Zaritsky, D., & Rix, H.-W. 1997, ApJ, 477, 118
Zolotov, A., Willman, B., Brooks, A. M., et al. 2009, ApJ, 702, 1058